Geology and emplacement history of the Nuevo Rosarito plutonic suite in the southern Peninsular Ranges batholith, Baja California, México

Tomás Alejandro Peña-Alonso[1,*], Luis Alberto Delgado-Argote[1], Bodo Weber[1], Fernando Velasco-Tapia[2], and Víctor Valencia[3,4]

[1] Departamento de Geología, CICESE, 22800 Ensenada, Baja California, Mexico.
[2] Facultad de Ciencias de la Tierra, Universidad Autónoma de Nuevo León, 67700 Linares, Nuevo León, Mexico.
[3] Department of Geosciences, University of Arizona, Tucson AZ, 85721, United States of America.
[4] Valencia Geoservices, 3389 N River Rapids Dr, Tucson AZ, 85712, United States of America.
** alepena@cicese.mx, topeax@gmail.com*

ABSTRACT

The Cretaceous Nuevo Rosarito plutonic suite is located in the southern part of the Peninsular Ranges batholith (~28.7 °N). It is hosted by a suite of Jurassic granitoid rocks dated at 151.6 Ma (U-Pb single zircon ages) and by Late Jurassic - Early Cretaceous volcanic and volcaniclastic rocks. Host rocks display solid-state fabrics related to a deformational event that occurred before the emplacement of the Nuevo Rosarito plutonic suite. The composition of the suite ranges from gabbro to granite. The suite is sub-alkaline and it is divided into three mafic and four felsic units. The geochemical composition of the felsic units varies from metaluminous to peraluminous, and shows arc-related geochemical signatures. Structural and geochemical data suggest that the emplacement of the plutonic suite took place in two episodes. The first one is defined by the intrusion of mafic units in which dioritic bodies were emplaced within a gabbroic body along NNE-SSW oriented extensional fractures. The second episode is defined by the intrusion of three felsic units during a NE-side up, syn-emplacement movement that occurred around 108.4 Ma.

Keywords: geochemistry, geochronology, deformation, emplacement, Peninsular Range batholith, Mexico.

RESUMEN

La serie plutónica Nuevo Rosarito del Cretácico se localiza en la parte sur del batolito de las Sierras Peninsulares (~28.7 °N). Está encajonada por granitoides jurásicos fechados en 151.6 Ma (edad U-Pb en zircones individuales) y por rocas volcánicas y volcanoclásticas del Jurásico Tardío – Cretácico Temprano. Las rocas encajonantes presentan fábricas de estado sólido relacionadas a un evento de deformación que ocurrió antes del emplazamiento de la serie plutónica. La composición de la serie varía de gabro a granito. La serie, que es subalcalina, se divide en tres unidades máficas y cuatro félsicas. La composición geoquímica de las unidades félsicas varía de metaluminosa a peraluminosa y muestra firmas geoquímicas relacionadas a arco. A partir de datos estructurales y geoquímicos se sugieren dos episodios de emplazamiento. El primero está definido por la intrusión de unidades máficas en donde

cuerpos dioríticos fueron emplazados dentro de un cuerpo gabróico a través de fracturas de extensión. El segundo episodio está definido por la intrusión de tres unidades félsicas durante un movimiento del bloque NE hacia arriba, simultáneo al emplazamiento, que ocurrió a ca. 108.4 Ma.

Palabras clave: geoquímica, geocronología, deformación, emplazamiento, Batolito de las Sierras Peninsulares, México.

INTRODUCTION

The Peninsular Ranges batholith (PRB) is a continuous belt of Late Cretaceous plutons that crops out from southern California, USA, to the northern half of the Baja California peninsula, Mexico. According to geochemical, mineralogical, geophysical, and age data (*e.g.*, DePaolo, 1981; Todd and Shaw, 1985; Gromet and Silver, 1987; Silver and Chappell, 1988; Gastil *et al.*, 1994; Tulloch and Kimbrough, 2003), it is a general convention to divide axially the batholith into a western and an eastern zone. The western zone is characterized by I- type plutons (Walawender *et al.*, 1990) related to an oceanic arc and emplaced at sub-volcanic depths (Johnson *et al.*, 2002). Most of the plutons of the western zone intrude Albian-Aptian volcanic and volcaniclastic intra-arc assemblages associated with the Alisitos Formation (Gastil *et al.*, 1975; Beggs, 1984; Busby *et al.*, 2006). The eastern zone is characterized by younger I- and S-type plutons related to a Late Cretaceous, eastward-migrating arc (Gromet and Silver, 1987) that intruded Ordovician to Permian continental clastic assemblages, as well as Proterozoic to Permian carbonate-siliciclastic assemblages (Gastil and Miller, 1984; Gastil, 1993). Between the western and eastern zones, a transitional zone has been described in several areas as distinct Triassic(?)-Cretaceous clastic and volcaniclastic flysch-like assemblage of uncertain tectonic origin (Figure 1a; Schmidt *et al.*, 2002).

Intense ductile deformation found in areas like the Sierra San Pedro Mártir and Calamajué (localities SSPM and 5, respectively, in Figure 1a), in the eastern edge of the western zone and within the transitional zone, suggests that the Alisitos arc was accreted along the southwestern North American continental margin *ca.* 115–108 Ma (Johnson *et al.*, 1999).

Most studies of plutons within the PRB are concentrated between southern California, and the latitude of El Rosario area in Baja California (Figure 1; locality 6). For example, in the El Rosario area, PRB plutons are hosted by the Cretaceous Alisitos Formation (Busby *et al.*, 2006). Few other studies have been conducted south of this region, especially in the El Arco area (Figure 1a, locality 10), which has been recognized as the southernmost exposure of the PRB (Schmidt *et al.*, 2002). In contrast to the geology reported in the El Rosario area, El Arco is a Middle Jurassic porphyry copper deposit (Valencia *et al.*, 2006) emplaced in a primitive oceanic crust environment (Weber and López-Martínez, 2006) that can be correlated with Jurassic magmatic sequences of the Cedros Island and the Vizcaino peninsula (Kimbrough and Moore, 2003; Hickey, 1984; locality 11).

Another important sequence to consider is the Eugenia Formation. This is represented by Late Jurassic-Cretaceous rocks outcropping in the Vizcaíno peninsula and the Cedros Island as well (Hickey, 1984). It has been proposed that this formation was derived from the San Andrés volcano-plutonic complex (Barnes, 1984), which, in turn, is contemporaneous to the flysch-like assemblages of the PRB transitional zone and to the Alisitos Formation.

The study area consists of a plutonic suite that intrudes prebatholithic undifferentiated metamorphic rocks (Figure 1b). However, northwestward from the study area, the prebatholithic rocks consist of volcanic and volcaniclastic rocks of the Early Cretaceous Alisitos Formation, which have been described by Beggs (1984) around the locality of Punta Prieta (Figure 1b). Similarly, volcaniclastic rocks including fragments of fossiliferous limestone crop out about 10 km north of the study area.

In order to define the relationships between plutonic rocks of the southern PRB and contrasted sequences of prebatholithic rocks, we conducted a comprehensive geological study that includes field work, structural, petrological, geochemical and geochronological analyses in the plutonic suite that has been labeled as the Nuevo Rosarito plutonic suite.

GEOLOGICAL BACKGROUND

The Nuevo Rosarito plutonic suite is located between 28.66 °N and 28.59° N, near the Pacific coast of Baja California (Figure 1). It comprises a northern and a southern part, which share the same lithology and field relationships, but have different geometries and their rocks exhibit drastic textural and mineralogical variations. The northern part consist of a 15 km^2 elliptical body elongated in a NNW-SSE direction, while the southern part consist of a 7 km^2 circular body with a dome-like shape that includes host rocks screens as large as 150 m^2 (Figure 2a).

Under the premise that plutons are composite bodies usually assembled by several individual magma pulses (*e.g.*, Coleman *et al.*, 2004; Vigneresse, 2004; Matzel *et al.*, 2006; Kemp *et al.*, 2007; Michel *et al.*, 2008), we identified seven different intrusive units that altogether comprise the Nuevo Rosarito plutonic suite. This suite is dominated by mafic rocks. The older and most widely exposed intrusive unit consists of

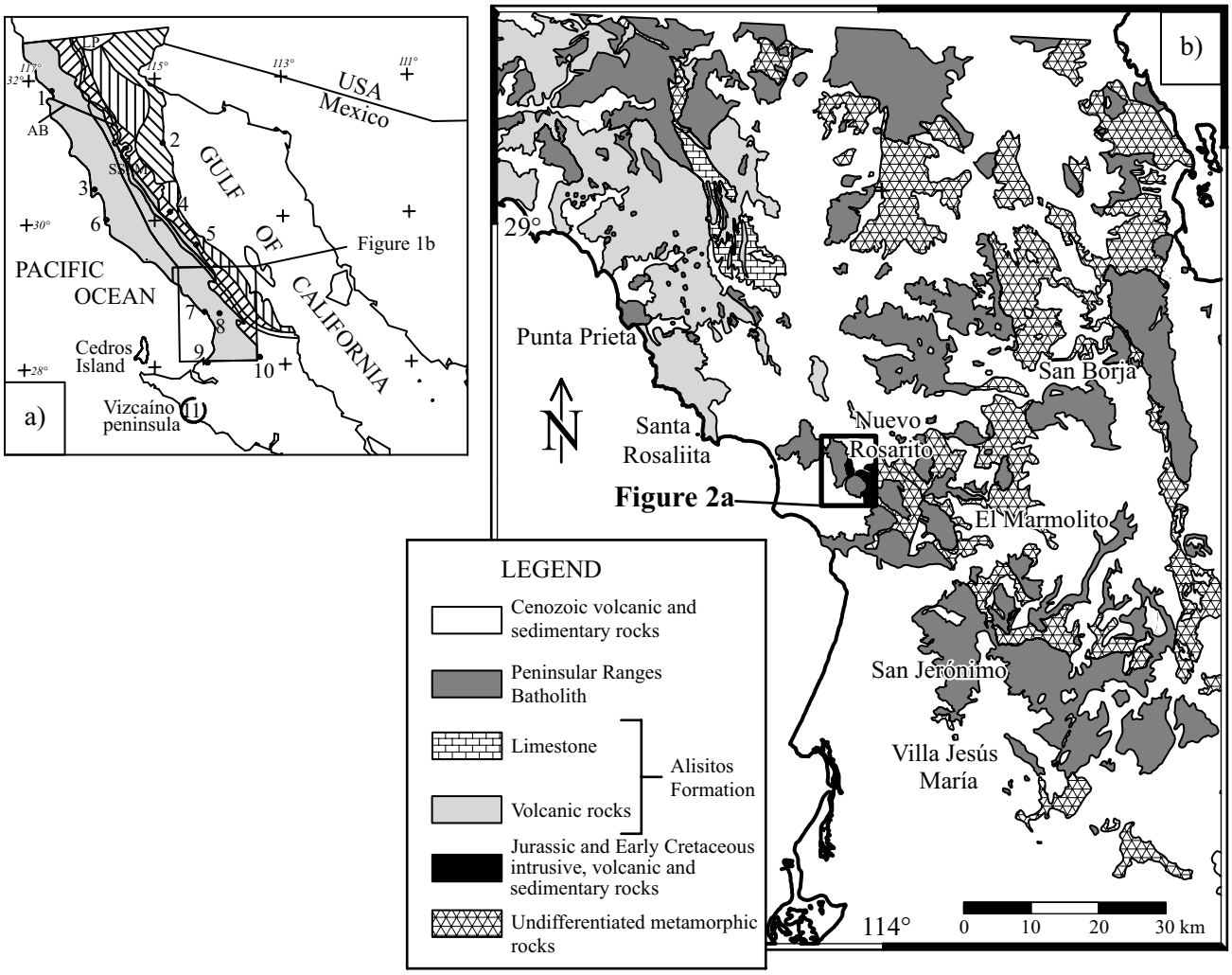

Figure 1. (a) Distribution of the distinct basements in the northern part of the Baja California peninsula and the Peninsular Ranges batholith (modified from Schmidt *et al.*, 2002). Hatched belts: from the top-left corner to the bottom-right corner: Proterozoic-Permian miogeoclinal carbonate-silicic assemblage; vertical: Ordovician-Permian slope-basin clastic assemblage; from the top-right corner to the bottom-left corner: Triassic(?)- Cretaceous volcaniclastic and clastic (flysch-type?) assemblage; grey solid: Cretaceous arc volcanic and volcaniclastic rocks. The two solid lines that axially divides the Baja California peninsula delineates the magnetite-ilmenite line from Gastil *et al.* (1990). Localities for reference: 1: Ensenada; 2: San Felipe; 3: San Quintín; 4: El Mármol; 5: Calamajué; 6: El Rosario; 7: Santa Rosaliita; 8: Nuevo Rosarito; 9: Guerrero Negro; 10: El Arco; 11: San Andrés volcano-plutonic complex; LP: La Posta pluton; AB: ancient Agua Blanca fault; SSPM: Sierra San Pedro Mártir. (b) Simplified geologic map of the central Baja California peninsula (modified after Martín-Barajas and Delgado-Argote, 1996; Delgado-Argote, 2000; Camarena-García, 2006). The undifferentiated rocks of Figure 1b are presumably pre-batholitic units of Jurassic-Early Cretaceous age.

two-pyroxene gabbro. The gabbro is cut by smaller intrusions of a two-pyroxene diorite (Kd) and a hornblende-pyroxene quartz diorite (Kqd). All these lithologies are intruded, in turn, by younger felsic dikes. Moreover, these dikes can be divided according to field relationships, mineralogy, texture, and geochemical composition into four distinct intrusive units: Kt (hornblende-biotite tonalite), Kg1 (biotite-hornblende tonalite-granodiorite-granite), Kg2 (hornblende-clinopyroxene granite-monzogranite-syenogranite) and Kg3 (biotite granite), in that chronological order.

In the following sections, the lithology and the structural patterns of the northern and southern parts of the Nuevo Rosarito plutonic suite and their host rocks are described. The emplacement conditions are interpreted from petrography and microstructure analyses, whereas igneous processes are elucidated from geochemistry. Furthermore, U-Pb ages of zircons from host rock units are reported here for the first time, together with an age of a hornblende-biotite tonalite from the central part of the plutonic suite.

HOST ROCKS

The host rocks of the Nuevo Rosarito plutonic suite are grouped into five lithologic units (Figure 2a): granitoid rocks (Jt), metamorphosed quartzfeldespatic volcanic and volcaniclastic rocks (Jv), amphibolitic rocks (Jma), hornfels (Kmh), and clastic rocks (Js).

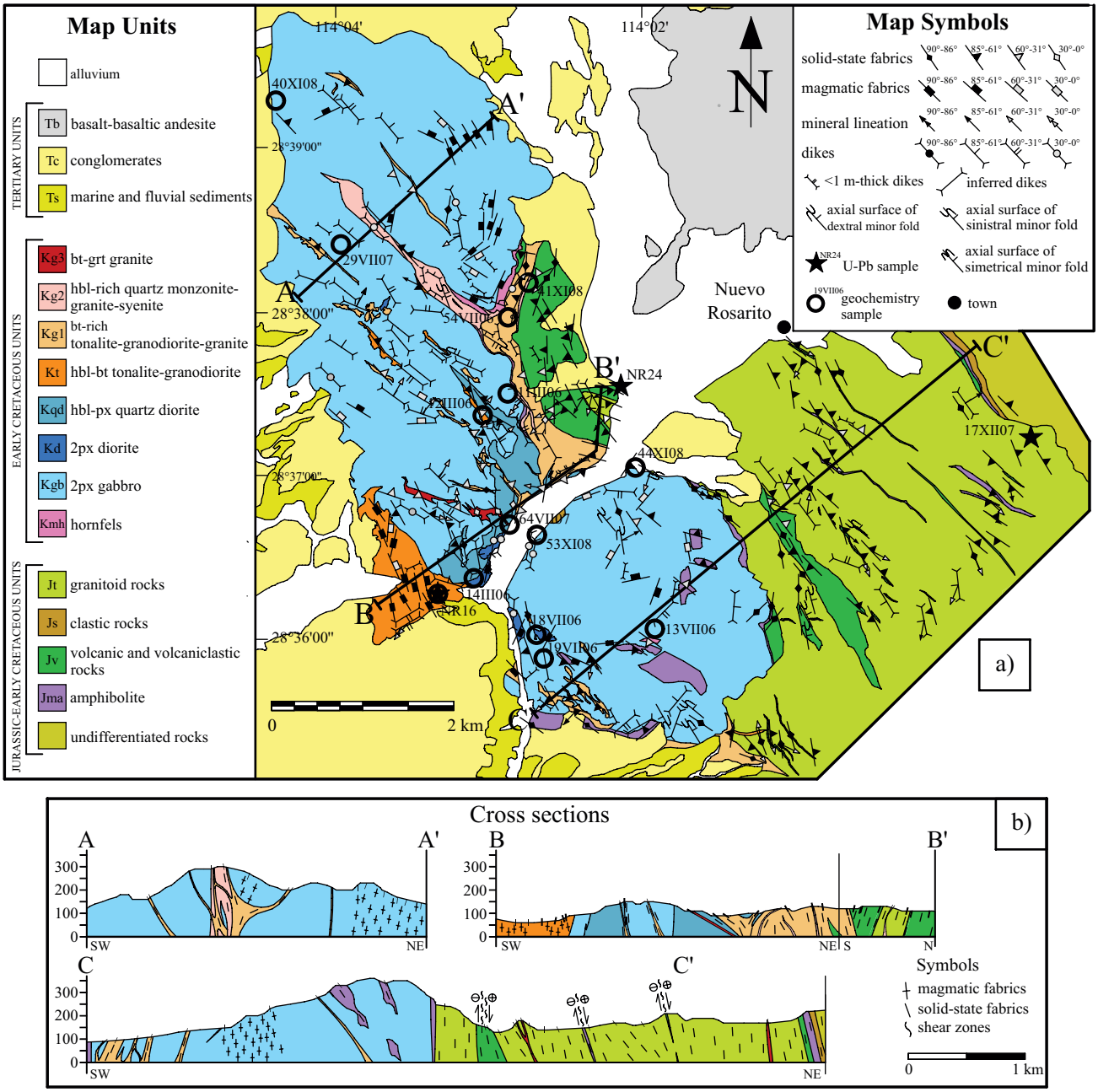

Figure 2. (a) Geologic map of the Nuevo Rosarito plutonic suite. The Nuevo Rosarito plutonic suite is divided by the Rosarito drainage into the northern (elongated) and southern (circular) part. Dikes with widths up to 5 meters are represented as elongated areas, while dikes with widths down to 5 meters are represented with a dike symbol. Solid-state fabrics include schists, protomylonites and mylonites. The base map is from CETENAL (1977). (b) Schematic cross sections of the Nuevo Rosarito plutonic suite. The shear zones in the section C-C' are related to the solid-state fabrics of the screens within the granitoid rocks (Jt), and are interpreted to be formed under a transpressive regime that occurred before the emplacement of the Nuevo Rosarito plutonic suite.

The granitoid rocks (Jt unit) are widely exposed in the southeastern part of the study area. They are medium to coarse-grained rocks that according to their mineralogy vary from tonalite to granodiorite. They also display protomylonitic to mylonitic fabrics and cm-scale aplitic dikes as well as quartz veins. The Jt unit usually contains screens of Jv and Jma rocks that have a nearly vertical attitude and sizes ranging from a few cm up to 600 m long.

In the northern part of the suite, the volcanic and volcaniclastic rocks of the Jv unit are mostly formed by andesitic to dacitic feldspar-rich porphyritic lava flows showing a greenschist facies mineralogy. They are composed of abundant euhedral to subhedral, feldspar phenocrysts (0.5 to 1.5 mm) in a very fine-grained, quartzfeldspatic, biotite>hornblende matrix. The Jv unit includes horizons of flow breccias formed by matrix-supported, cobble-sized

fragments of mafic and felsic intrusive rocks, and protomilonitic rocks of andesitic flow breccias and fine-grained volcaniclastics. These protomilonitic rocks are located near the NR24 sample site (Figure 2a). Another feature of the Jv unit from the northern part of the suite is that it is in contact with chloritized coarse-grained hornblende-biotite tonalitic rocks that show schistose to protomylonitic fabrics and that locally contain a few m-thick screens of felsic protomylonites and amphibolites. Here we hypothesize that such tonalitic rocks are part of the widely exposed Jt unit located on the southern part of the suite; however, this idea remains to be tested.

In the southern part of the suite, the Jv unit is made up by andesitic and rhyolitic lava flows, volcanic breccias, and felsic tuffs. Mafic schists and orthogneisses are also present. Some portions of these Jv volcanic units display dynamic recrystallization and protomylonitic texture. In the eastern side of the study area, near the sample site 17XII07, clastic rocks (Js) are apparently interstratified with protomylonites of volcanic breccias that include granitoid fragments and tuffaceous material.

Amphibolitic rocks (Jma; Figure 2a) parallel the foliation of the granitoid unit Jt and crop out as large lens-like screens in the eastern margin of the study area or as isolated rock screens within the gabbroic rocks (Kgb). Their typical mineral assemblage is plagioclase+hornblende+actinolite± biotite±epidote.

Along the western contact with the gabbroic rocks of the northern part of the suite, the host rocks developed a 10 to 100 m-wide contact aureole that is characterized by hornblende-hornfels and pyroxene-hornfels facies (Kmh; Figure 2a). The mineralogy of the hornblende-hornfels is plagioclase+hornblende+clinopyroxene+opaques±quartz in a fine-grained texture. The pyroxene-hornfels, in turn, is formed by an assemblage of plagioclase+orthopyroxene +clinopyroxene+opaques±biotite±hornblende, having a medium to coarse-grained granoblastic texture. A subvertical penetrative schistosity developed on the Jv volcanic rocks and the Kmh hornfels of the northern part of the suite, parallel to the contact aureole, is sometimes destroyed by younger Kg1 and Kg2 felsic bodies.

The intensity of the fabrics and the structural patterns of the host rocks of the northern part of the suite are strongly different from those of the southern one. On the one hand, in the northern part of the suite, the host rocks have solid-state fabrics ranging from schistose to protomylonitic. Moreover, average foliation and bedding dips towards the SW (mean 150º/60ºW; Figure 3a). In addition to that, the protomylonitic rocks exhibit a well-developed SW-dipping stretching lineation that is oriented towards 228º/58º in average (Figure 3a). On the other hand, in the southern part of the suite, host rock bedding and deformational fabrics are sub-vertical and NNW oriented (mean 342º/83ºE; Figure 3b). The Jv volcanic host rocks display intense deformational fabrics, defined by penetrative schistosity and/or asymmetric porphyroclast tails in the lava-like rocks, and by elongated fragments in the volcanic breccias. Furthermore, well-developed stretching lineations in biotite from granitoids, and lineation of quartz exhibited by some volcanics are nearly vertical or dip toward SE (Figure 3b). All those patterns are also present in the host rock screens contained within the gabbroic rocks (which indicates that their deformational fabrics were developed prior to the gabbro emplacement). Another difference between the northern and southern part of the suite is that the circular geometry of the southern part of the suite locally controls the schistose fabrics of the surrounding host rocks.

THE NUEVO ROSARITO PLUTONIC SUITE

Melanocratic two-pyroxene gabbro (Kgb) show coarse- to medium-grained textures, and commonly exhibits 6 cm to 2 m thick layers defined by granulometric variations of the plagioclase. In the southern part of the suite, the gabbro locally displays cm to m-scale cumulitic layers composed of mm to 2 cm-euhedral plagioclase phenocrysts (Figure 4a). Along the contacts with the host rock screens, the Kgb unit shows magmatic fabrics defined by cm-wide compositional banding. Also, they usually preserve vertical primary fractures oriented towards NW-SE and NE-SW (Figure 3c).

In the northern part of the suite, two-pyroxene diorite (Kd) crop out as bodies of less than 100 meters long and as cm-scale dikes as well. Diorite is cut by abundant amphibole veins of probable hydrothermal origin (dioritic enclave in Figures 4b and 4c). However, in the southern part of the suite, diorite crops out as 2 to 20 m-wide bodies of interfingered geometry and with jagged-like contacts (Figure 4d), as well as 3 to 50 cm-thick dikes displaying smoothly curviplanar contacts. The interfingered Kd bodies and dikes are persistently oriented towards NNE throughout the suite (mean 21º/85ºSE, Figure 3d).

The geometry of a hornblende-pyroxene quartz diorite (Kqd) that crops out in the central portion of the study area is obscured by the intrusion of younger felsic bodies (Kt, Kg1, Kg2, and Kg3 in Figure 2a). This unit includes subangular enclaves of the two-pyroxene diorite (Kd) suggesting that it postdates Kd. Occasionally, quartz diorites have NW-SE oriented solid-state fabrics indicated by the elongation of amphiboles and cm-scale shear bands.

The gabbro (Kgb), diorite (Kd) and quartz diorite (Kqd) units are intruded by a medium- to coarse-grained, hornblende-biotite tonalitic-granodioritic unit (Kt). This unit crops out in the southwestern portion of the study area as a massive body of approximately 800 m^2 or like NW-SE oriented dikes in the northern part of the suite. The Kt massive body shows numerous angular to subrounded, cm- to dm-scale dioritic autoliths and enclaves (Figures 4b and 4c), and displays well-preserved vertical magmatic fabrics defined by the alignment of minerals, by local schlieren-type banding, and by the alignment and/or elongation of dioritic

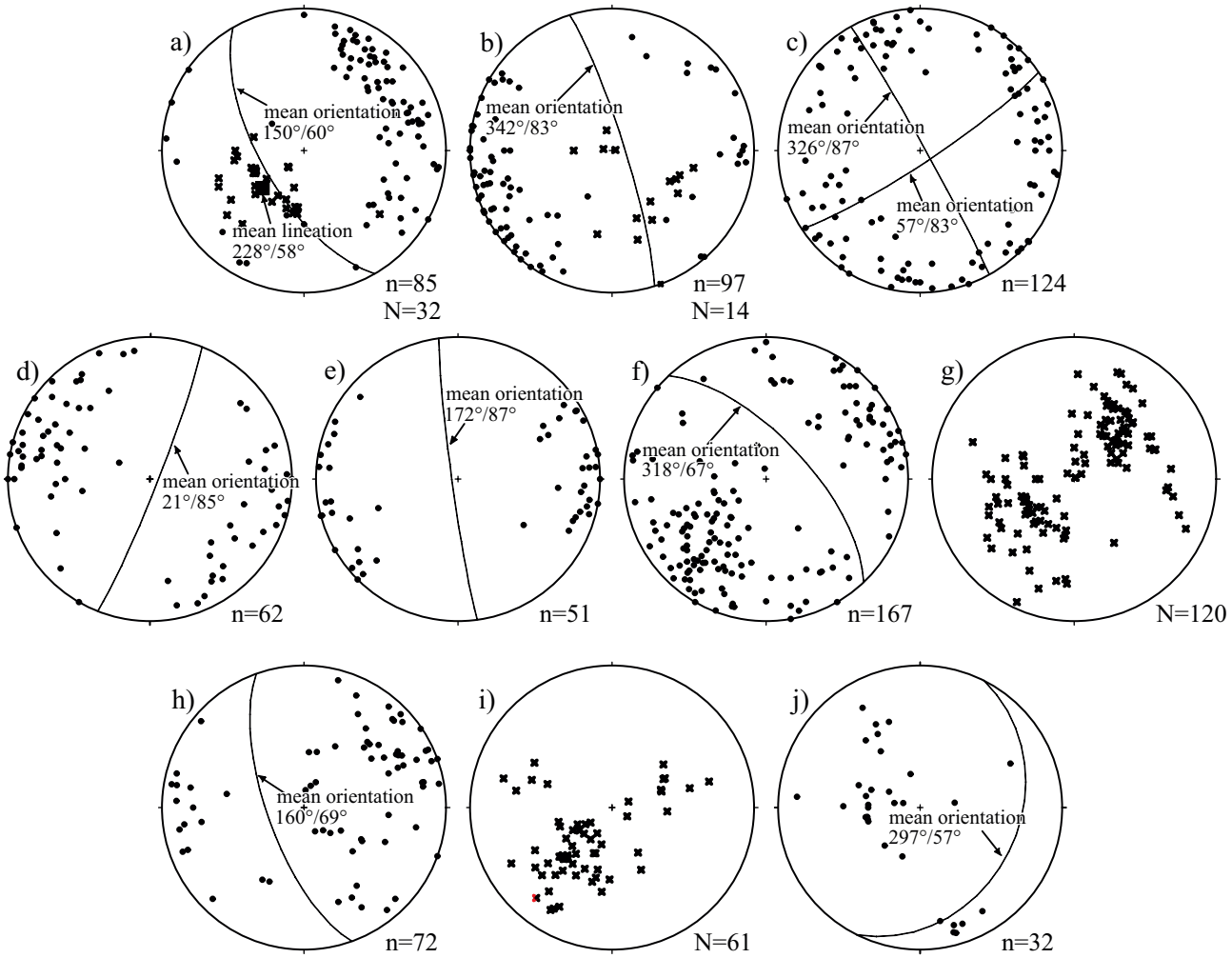

Figure 3. Structural patterns of the Nuevo Rosarito plutonic suite; solid-state fabrics poles, host rocks bedding and orientation of planar intrusives are represented by solid circles; mineral and stretching lines are represented by crosses. a) solid-state fabrics (including bedding) and lineation of the host rocks of the northern part of the suite; (b) solid-state fabrics (including bedding) and lineation of the host rocks of the southern part of the suite; (c) vertical fractures developed in the gabbroic unit (Kgb); (d) orientation of the diorite dikes (Kd) and their main magmatic fabrics; (e) magmatic fabrics of the massive Kt body located in the northern part of the suite; (f) orientation of the Kt and Kg1 dikes and their solid-state fabrics; (g) lineation displayed in the Kt and Kg1 dikes; (h) orientation of the Kg2 dikes and their internal solid-state fabrics; (i) lineation displayed in the Kg2 dikes; (j) orientation of the Kg3 dikes and their internal lineation. n: data of fabrics and orientation of intrusive bodies, N: data of lineation.

enclaves and autoliths (mean 172º/87ºW; Figure 3e). In contrast, the Kt dikes exhibit magmatic fabrics delineated by mineral alignment, and overprinted by schistose textures.

Following the sequence of emplacement, the Kt unit is intruded, in turn, by a series of dikes showing single and sheeted geometries. Their modal composition varies from tonalite to granite (Kg1 unit) or from granite to syenogranite (Kg2 unit). Both Kg1 and Kg2 units show imbricate contact relationships suggesting a penecontemporaneous emplacement.

The Kg1 unit represents white to light gray, biotite-rich bodies showing sheeted-like geometries or cropping out as single cm- to m-thick dikes following a NW orientation. The sheeted-like Kg1 bodies have porphyritic to granular texture, and display local schistosity paralleling dm-scale Kg2 dikes (Figures 4e and 4f). However, Kg1 dikes exhibit intense solid-state fabrics (Figure 4g) dominated by mylonitic textures (Figures 4h and 4i). They can also contain ductile deformed mafic xenoliths or host rock enclaves oriented subparallel to the foliation.

The Kg2 unit represents pink-colored, hornblende-rich dikes ranging from few decimeters to 1 m in thickness exhibiting internal compositional banding and mm-scale miarolitic cavities. In the northern part of the suite they have sheeted geometries containing cm-scale Kg1 dikes and lenses of mafic rocks, whereas in the southern part they crop out as single dikes.

The mafic rocks in the immediate vicinity of Kg1 and Kg2 units usually display ductile features (Figures 4h and 4i). The internal fabrics of the Kt dikes and the Kg1 bodies are oriented towards NW-SE (Figure 3f), exhibiting stretching lineation dipping SW and NE in average (Figure 3g).

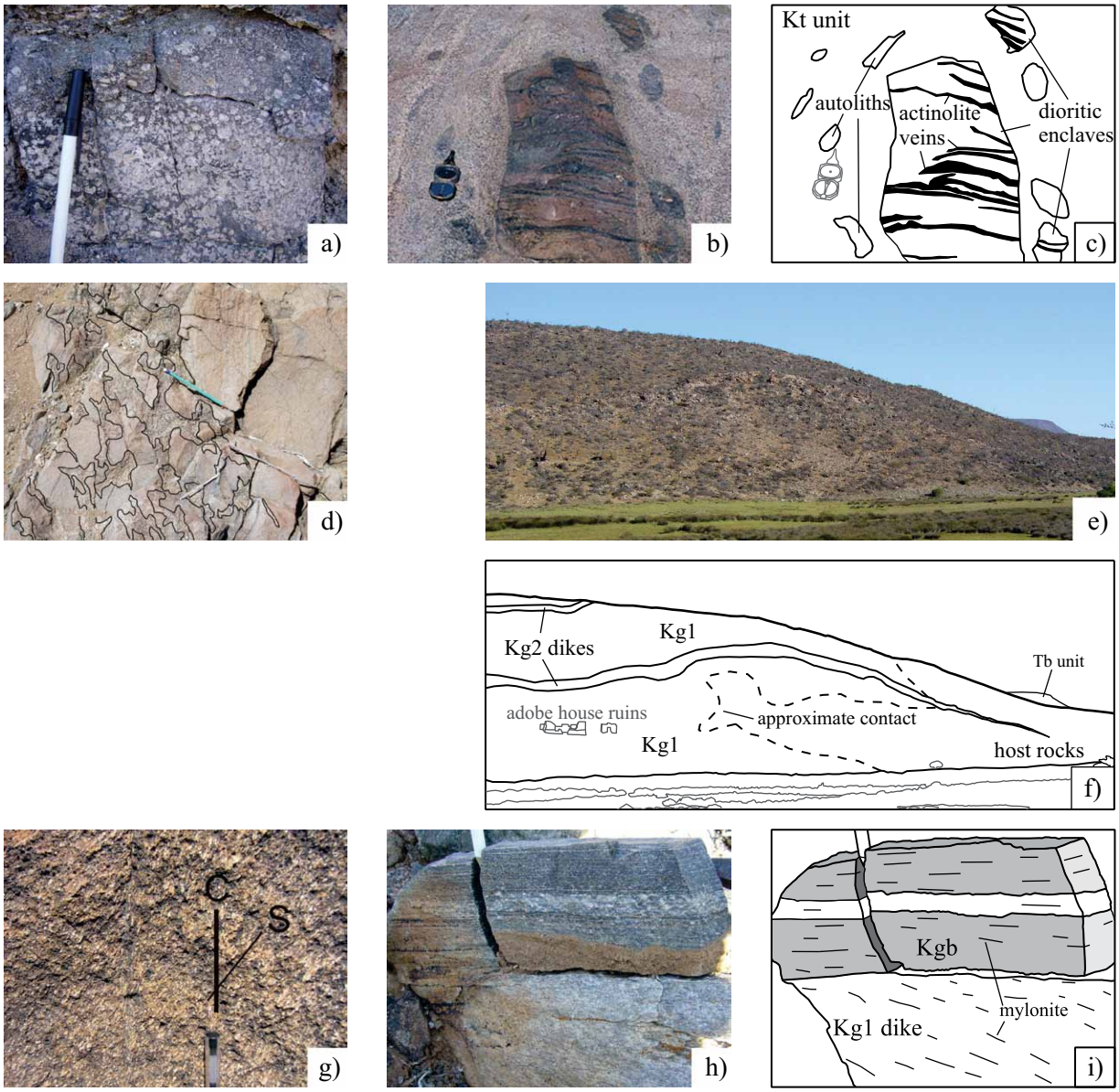

Figure 4. Outcrops of the Nuevo Rosarito plutonic suite. (a) Coarse-grained plagioclase cumulates in gabbro from the southern part of the suite; (b) and (c) Plan view of dioritic enclaves (Kd unit) contained in the Kt massive body; (d) Plan view of the contact zone between coarse-grained gabbro and the fine-grained interfingered dioritic body; (e) and (f) Kg1 unit in the eastern side of the northern part of the suite intruded by hornblende-rich Kg2 dikes; (g) Kg1 dike with internal S-C structures delineated by its whole mineral foliation; (h) and (i) Contact between a mylonitized Kg1 dike (lower half) and gabbro (upper half) where internal fabrics of the felsic dike are oblique with respect to the dike margins.

In contrast, the Kg2 bodies are mainly oriented SE (Figure 3h), developing a SW directed lineation (Figure 3i). Nine kinematic indicators were obtained from the Kt dikes, and the Kg1 and Kg2 bodies: two from outcrops (as the S-C structures from Figure 4g), and seven from thin sections oriented parallel to the XZ plane. Those kinematic indicators invariably indicate a northeast side up sense of shear.

The last unit in the emplacement sequence is composed of cm to m-thick aplitic dikes of biotite granite (Kg3 unit) that include pegmatite facies concentrated at their margins or along their axial planes. These dikes are mainly NE-SW oriented (Figure 3j).

PETROGRAPHY AND MICROSTRUCTURES OF THE NUEVO ROSARITO INTRUSIVE UNITS

Two-pyroxene gabbro (Kgb)

As shown in the modal classification of Figure 5a, seven of the eleven samples of the gabbroic rocks plot in the gabbronorite field. They display hypidiomorphic textures, showing seriated, euhedral to anhedral labradorite-andesine (40–62 %) typically exhibiting a normal zonation. Orthopyroxene (4–29 %) is coarse-grained, granular to subophitic. Subophitic augite (4–27 %) is medium to

coarse-grained. Opaque minerals can reach 12 % of total mineral content. The cumulitic textures of the southern part of the suite are made up by 90–98 % coarse-grained labradorite that can exhibit reaction rims. Additionally, augite commonly exhibits rope-type pigeonite exsolution lamellae and minor inverted pigeonite. Also, plagioclase crystals occasionally have trachytoid textures. At the contacts with the Kd interfingered bodies (Figure 4d), up to 34 % of the Kgb pyroxene content is partially replaced by green-brown hornblende.

At two locations, where deformed gabbro occurs in the immediate vicinity of the felsic dikes, the gabbro is metamorphosed under greenschist (albite+quartz+actinolite±biotite±epidote±oligoclase) to amphibolite (sodic plagioclase+hornblende±epidote±clinopyroxene) facies conditions.

Two-pyroxene diorite (Kd)

Diorite is commonly alliotromorphic granular. Its modal composition is defined by andesine (51–55 %), fine to medium-grained subophitic enstatite (7–25 %), augite (10–13 %), minor brown-poikilitic or green-interstitial hornblende (4–17 %), and opaque minerals (6–12 %).

In the southern part of the suite, dioritic rocks in contact with gabbro commonly contain calcic plagioclase xenocrysts, which composition is highly similar to the gabbroic plagioclase. In addition, the contact between interfingered diorite and gabbro (Figure 4d) is microscopically delineated by the crystalline margins of plagioclase grains from the gabbro (Figure 6a). Both observations define an interlocking texture as described by Hibbard and Waters (1985), suggesting late magmatic fracturing.

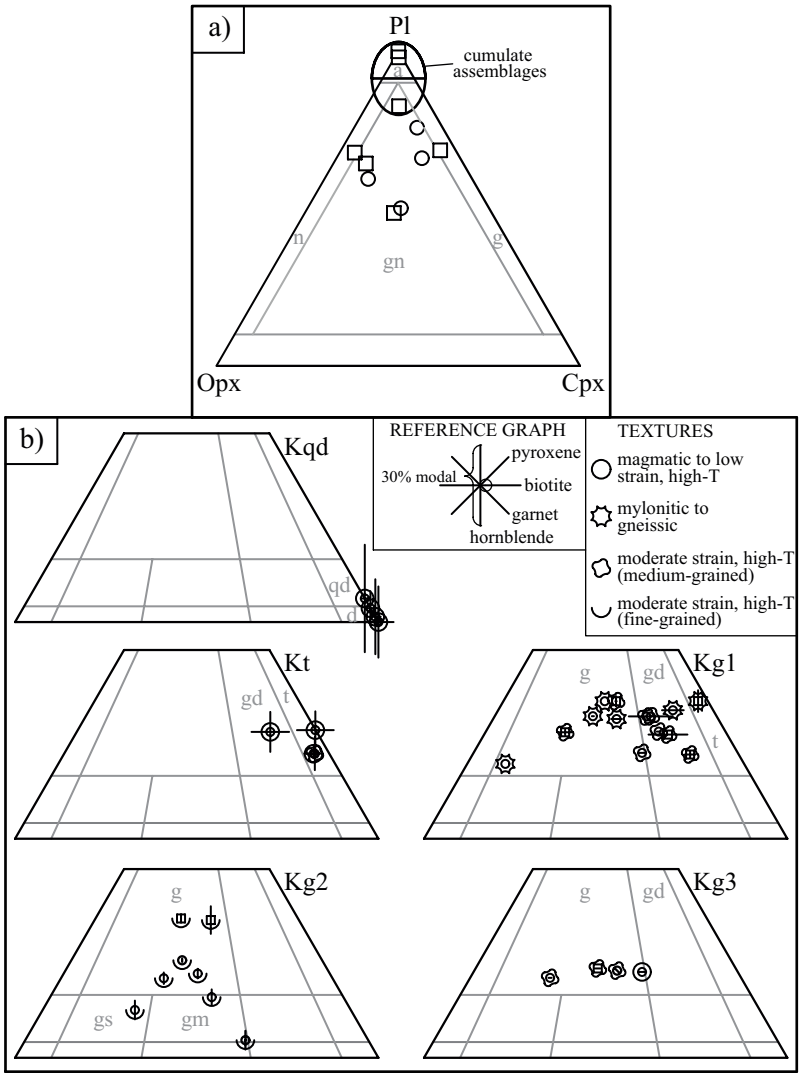

Figure 5. (a) Pl-Opx-Cpx modal classification of gabbro (Kgb unit) after Streckeisen (1976). Circles and squares are samples from the northern and the southern part of the suite, respectively. (b) QAP modal classification (after Streckeisen, 1976) indicating main varietal minerals and textures. The longitude of the bars in the reference graph of varietal minerals represents 30% modal content. Abbreviations: a: anortosite, n: norite, gn: gabbronorite, g: gabbro, d: diorite, qd: quartz diorite, t: tonalite, gd: granodiorite, g: granite, s: syenite, qm: quartz monzonite. Circles and squares represent samples from the northern and the southern part of the suite, respectively.

Hornblende-pyroxene quartz diorite (Kqd)

Most of the quartz dioritic rocks show seriated medium to coarse-grained, hypidiomorphic and allotriomorphic textures composed of andesine (52–79 %), intergranular quartz showing undulatory extinction (<4 %), subophitic green hornblende with occasional inclusions of augite (13–41 %), reddish brown biotite (3–4 %), and opaque minerals (1–3 %). Few analyzed samples include minor hypersthene grains (<3 %). Numerous plagioclase grains are discontinuously normal zoned and show highly fractured, boxy-like calcic cores with convoluted rims that are indicative of core resorption.

Hornblende-biotite tonalite (Kt)

The massive body of this unit is formed by coarse- to medium-grained, hypidiomorphic rocks, whereas dikes are usually allotriomorphic. This unit is composed of oligoclase (37–62 %) commonly displaying discontinuous normal and oscillatory zonation; potassic feldspar (<12 %) with subophitic texture usually displaying tartan twinning; fine-grained quartz (23–25 %) with incipient chessboard undulatory extinction (Figure 6b); green hornblende (2–15 %) with intergranular fractures; intergranular to intragranular red-brown biotite (up to 14 %) exhibiting misoriented segments or kinking; and opaque minerals (up to 2%). Zircon and apatite occur as accessory minerals. Kt dikes can exhibit incipient S-C structures and myrmekite intergrowth in the potassic feldspar grains.

Biotite-rich tonalite-granodiorite-granite (Kg1)

This unit has compositions ranging from biotite tonalite to potassic feldspar-rich granite (Figure 5b), containing oligoclase (10–49 %), potassic feldspar (10–66 %), quartz (24–40 %), biotite (<16 %), and opaque minerals (<1 %). Zircon, apatite, and tourmaline can also be present as accessory minerales. In the southern part of the suite, this unit also contains hornblende (2–8 %).

The internal fabrics of the Kg1 dikes are mainly mylonitic, defined in the microscale by feldspar, quartz and/or hornblende porphyroclasts wrapped by fine-grained, quartz and biotite-rich folia. The feldspar porphyroclasts display sigmoid shape, and moderate to intensively recrystallized grain margins (Figure 6c). Potassic feldspar porphyroclasts frequently exhibit tartan twinning and/or flame perthites. The quartz porphyroclasts are rounded, displaying undulatory or chessboard extinction. The hornblende porphyroclasts exhibit misoriented segments and boudinage (Figure 6d). Hornblende can also occur as recrystallized aggregates outlining the folia. The texture of the quartz of the folia (anastomose around the deformed porphyroclasts) suggests recrystallization by bulging or subgrain rotation mechanism.

Some samples include feldspar grains with intragranular fractures filled by late phases of albite or quartz

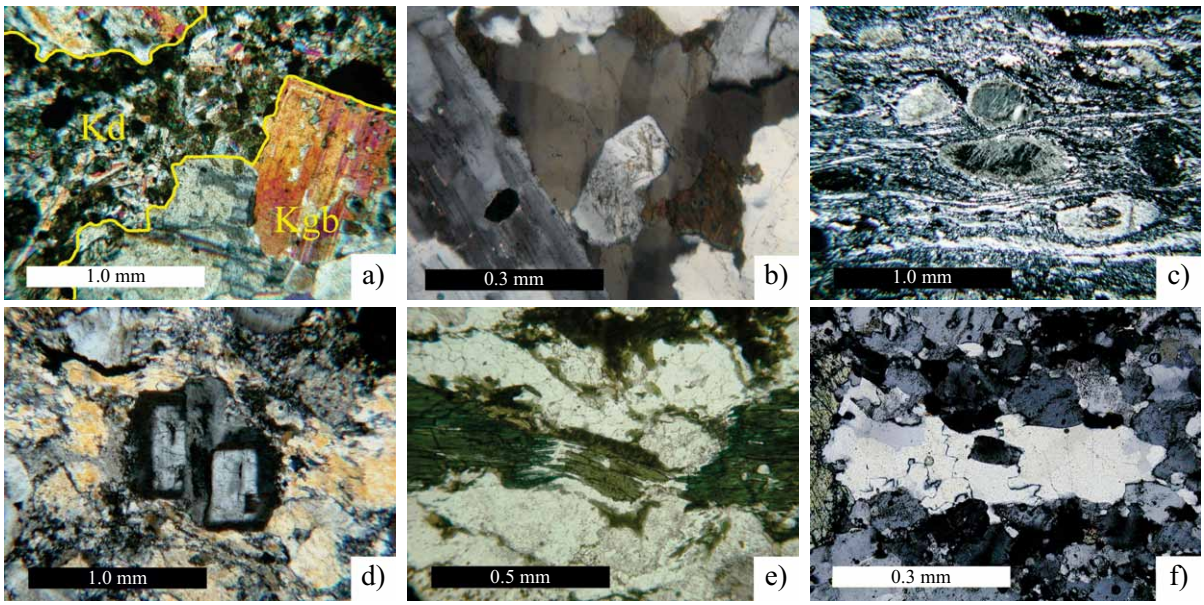

Figure 6. Some textures and microstructures of the intrusive units. (a) Contact between coarse-grained gabbro (Kgb) and fine-grained diorite (Kd) defining an interlocking texture (after Hibbard and Waters, 1985) (b) Coarse-grained quartz from the Kt massive body exhibiting incipient chessboard undulose extinction. (c) Overview of a thin section oriented parallel to the XZ plane from a Kg1 dike, indicating sinistral shear. Feldspar porphyroclasts have indented boundaries. This sample includes type 1-quartz ribbons (after Boullier and Bouchez, 1978) of polycrystalline aggregates obliquely oriented, from the lower-right corner to the upper-left corner. (d) Normal discontinuously-zoned plagioclase truncated by a late-phase filled-boundary, placed almost orthogonal to foliation (shortening direction), defining a contact melting microstructure (after Park and Means, 1996). (e) Boudinaged hornblende grain. (f) Elongated quartz grain with lobate boundaries and indentations, surrounded by aggregates of recrystallized plagioclase and potassic feldspar.

(submagmatic fractures after Bouchez *et al.*, 1992). We also report zoned plagioclase grains whose chemical zonation is truncated in high angles with respect to the foliation and healed by late-phases, which are in optical continuity with the outer rims (Figure 6e; fusion contact from Park and Means, 1996).

Hornblende-rich granite-monzogranite-syenogranite (Kg2)

The bodies from this unit are fine-grained, allotriomorphic granular, composed of subhedral to anhedral oligoclase displaying mechanical twinning and misoriented segments (21–47 %); anhedral potassic feldspar with tartan twinning and/or replaced by myrmekites (12–63 %); indented to lobular quartz (Figure 6f) with subgrains and undulatory to incipient chessboard extinction (6–43 %); and elongated green hornblende (sometimes boudinaged) paralleling the foliation (1–14 %). They also contain minor anhedral augite or pigeonite (trace–4 %), opaque minerals (trace–8 %), and a relatively high population of accessories (2–5 %), including apatite, tourmaline, zircon, sphene, rutile, and hematite.

Biotite granite (Kg3)

Dikes from this unit have hypidiomorphic to allotriomorphic granular textures. Oligoclase (21–45 %) shows normal zoning and mechanical twining; potassic feldspar (26–53 %) is present in perthites and mesophertites with a typical tartan twinning; and anhedral quartz grains (19–26 %) showing consertal textures and undulatory to incipient chessboard extinction. Other minerals present in this unit are intergranular biotite incipiently chloritized (2 %), minor white mica (<1 %), opaque minerals (<1 %), and apatite and zircon as accessory minerals (<1 %). Euhedral to subhedral almandine can reach up to 6 % volume content in the northern part of the suite.

WHOLE-ROCK GEOCHEMISTRY

Analytical and initial data handling procedures

Representative samples of all plutonic units, excepting Kqd, were selected to establish their major and trace element composition. Sample locations are shown in Figure 2a, whereas details of field description and petrographic features are summarized in Table 1.

Samples were initially processed at the Geology Department at CICESE using a Braun® iron-jaw crusher and a Bico® disk plate pulverizer to obtain grain sizes less than 1.0 mm. Following, representative aliquots of ~100 gr of rock powder were processed using a Bico® tungsten carbide ring pulverizer and stored in Nalgene® HDPE (high density polyethylene) bottles. Whole-rock major and trace element compositions were determined in ActLabs laboratories, Canada, by 4B or 4Litho analytical codes. Major and trace element compositions under 4Litho code, and major element compositions under 4B code, were determined by a lithium metaborate/tetraborate fusion procedure followed by an ICP-MS method. Trace element compositions under 4B code were determined by: (a) a total digestion procedure followed by ICP-MS analysis (Cu, Mo, Ni, S, Zn), (b) a lithium metaborate/tetraborate fusion procedure followed by ICP-MS analysis (Sr, V, Y, Zr), and (c) an instrumental neutron activation technique (As, Co, Cr, Hf, Rb, Sc, Th, U, La, Ce, Nd, Sm, Eu, Yb, Lu). CIPW norms were calculated considering an anhydrous 100% adjusted basis, with Fe_2O_3/FeO ratios adjusted according to SiO_2 content (Middlemost, 1989). All computations (anhydrous and iron-oxidation ratio adjustments, and CIPW norm compositions) were automatically done using the SINCLAS software (Verma *et al.*, 2003). Geochemical data were compiled and used to construct several variation and REE chondrite-normalized diagrams. Normalization REE data of chondrite were taken from Haskin *et al.* (1968) and Nakamura (1974).

Geochemistry

As expected, with the exception of alkalis, TiO_2 and P_2O_5, major element compositions decrease with increasing SiO_2 (for example MgO; Figure 7a). In contrast, (Na_2O + K_2O) content increases with SiO_2, showing a nearly linear pattern (Figure 7b). Sr also shows a marked decrease with increasing SiO_2 (Figure 7c), whereas Ba, Zr, and LREE display an opposite behavior (for example, Figure 7d). The rest of the trace elements are characterized by a lack of coherent trends in the variation diagrams.

Mafic units

Gabbroic rocks (Kgb; 42.9–47.5 wt % SiO_2) have high alumina (17.2–23.7 wt %) and moderate to high magnesium content (5.6–11.7 wt %). Most of the samples contain normative olivine (1.5–29.6 %) and hypersthene (0.8–13.5 %) with the exception of one sample that yielded normative nepheline (0.8 %). Gabbroic rocks are characterized by low concentrations of TiO_2 and P_2O_5 compared to the other units (Table 2). Chondrite-normalized REE abundances of the gabbroic rocks (Figure 8a) have 2 to 5 times the chondrite level, display relatively flat patterns (La/Yb_{CN} 0.5–1.5), and positive-Eu anomaly (Eu/Eu* 0.52). One sample has a negative Ce anomaly (gabbro 40XI08; Table 2), probably related to oxidation and secondary mobility of Ce. As pyroxene of this sample is moderately altered to uralite, particle scavenging hydrothermal activity (*e.g.*, Hongo *et al.*, 2007) may explain this anomaly.

Dioritic rocks (Kd; 49.3–50.2 wt % SiO_2) also have high alumina (18.2–18.4 wt %), and moderate magnesium content (5.2–5.8 wt %). Their CIPW norm is characterized

Table 1. Petrography and field description of the geochemically analyzed and U-Pb (zircon) dated samples.

Unit	Sample	UTM northing	UTM easting	Lithology	Petrography	Field setting
Kgb	29VII07	786701	3171684	2px gabbro	Hypidiomorphic granular; medium grained; lab>>and; subhedral hy occasionally with incipient misoriented segments; subophitic aug; PCO=58:28:12; acces, op.	Fresh medium grained sample; there are several felsic dikes with strong foliation 300 m north and northeast from this point. Magnetic.
Kgb	13VII06	790149	3167463	2px gabbro	Hypidiomorphic granular; medium grained; subhedral lab; subophiticanhedral hy; equigranular subhedral aug, and minor ol; PCO=49:27:34; acces, op.	Sample with magmatic layering parallel to stopped block (?) contact. Magnetic.
Kgb	11III06	788533	3170048	2px gabbro	Hypidiomorphic granular; medium grained; subhedral lab>>and; subhedral seriated hy, equigranular subhedal aug, and minor anhedral ol; PCO=50:26:24; acces, op.	Eastern margin of the southern part of the suite. Includes amphibole pots. Magnetic.
Kgb	44XI08	789936	3169234	2px gabbro	Hypidiomorphic granular; medium grained; anhedral lab slightly fracturated; sub-anhedral granular hy; sub-anhedral aug; minor interstitial hbl; PCO=69:4:27; acces, op.	Northern margin of the southern part of the suite. About hundred meters separated from a leucocratic intrusion.
Kgb	40XI08	786155	3173298	2px gabbro	Allotriomorphic granular; seriated; anhedral lab with intense intragranular actinolite-filled fractures and mechanical twinning; pyroxene moderately replaced by prh+act+chl; PP = 76:24.	Northern part of northern part of the suite. Few meters near discrete shear zone with intense sinuous fabrics in gabbro.
Kd	18VII06	788831	3167304	2px diorite	Allotriomorphic; fine grained; subhedral to anhedral and>lab, anhedral fine grained opx and cpx, and green poikilitic hbl; PCO=72:18:10; some pl suggest synneusis processes.	Complex interfingered diorite bodies in contact to coarse-grained gabbro. Both unit rocks are cut by amphibole veins. ~1 km west of 13VII06.
Kd	14III06	788161	3168018	2px diorite	Allotriomorphic; medium to fine grained; subhedral to anhedral lab<and>olg; some discontinuous normal zoning; equigranular eu to subhedral opx; equigranular sub to anhedral cpx; hbl present. PCO=61:28:11; acces, op, zr; some pl suggest synneusis processes.	Fine grained, brownish diorite outcrop with high content of amphibole veins in transitional contact to mingling tonalite-diorite zone.
Kt	NR16	787703	3167821	hbl-bt tonalite	Allotriomorphic granular; medium grained; acces op, zr, ap; QAP=27:4:69; moderate foliation; qtz with undulose extinction to square subgrains. Include chl, ep, and sph as alteration phases.	Outcrop of a mingling zone; foliation oriented ~NNW-SSE. Coarse-grained hbl-bt tonalite containing ~10cm rounded diorite enclaves. Tonalite with felsic bands.
Kt	12III06	788257	3169820	hbl-bt granodiorite	Porphyroclastic; medium-fine grained; acces op, zr, ap; P:M=58:42; qtz with undulose extinction to mortar texture; kfs with incipient tartan twinning; pl replaced by ep+wm+ab; hbl fracturated to boudinaged; bt brownish anastomosing around porphyroclasts.	Tonalite outcrop with overprinted magmatic and solid-state fabrics. In contact with undeformed mafic rocks of sample 11III06. Phenocrysts of pl and hbl.
Kg1	54VII06	786790	3170483	bt granite	Porphyroclastic; medium-fine grained; acces op, zr, ap; P:M=21:79; qtz in recrystallized ribbons; pl with normal and multiple zoning replaced by ep+wm+ab; bt and wm defining S-C structure.	Felsic dike ~4m-thick NW-SE oriented. Includes pl and kfs phenocrysts, with bt as the principal mafic phase. Intrudes mafic schists.
Kg1	19VII06	788929	3167138	bt-hbl grano-diorite	Allotriomorphic granular; medium to fine grained; acces op, zr, ap, tur; pl with normal and multiple zoning replaced by ep+wm; anhedral intergranular kfs with myrmekitic intergrowths; green subophitic hbl; brownish inter-intragranular bt. QAP=27:13:60.	Porphyritic felsic dike ~4m-thick. Includes qtz-rich en-echelon veins that display sinistral movement in plan view; their bt grains are highly elongated parallel to the dike orientation.

continues

Table 1 (continued). Petrography and field description of the geochemically analyzed and U-Pb (zircon) dated samples.

Unit	Sample	UTM northing	UTM easting	Lithology	Petrography	Field setting
Kg2	41XI08	788761	3171263	hbl-granite-syenite	Plagioclase-rich domain; allotriomorphic granular; fine grained; high population of acces op, ap, ar, tur; anhedral pl and kfs with lobate grain boundaries; anhedral qtz with new grains . QAP=25:14:61.	~10m wide body, with compositional banding of plagioclase-rich and potassic feldspar-rich domains including miarolitic cavities.
Kg3	53XI08	788854	3168494	bt granite	Allotriomorphic granular; medium-coarse grained; acces op, ap, zr; subhedral pl with normal zoning; kfs with low myrmekite population and/or incipient tartan twinning; anhedral qtz with incipient square subgrains. QAP=33:38:28.	Horizontal, fine-grained, aplitic-like dike ~3 m-thick. Sinuous margins, incipient schistose fabrics, exhibiting isofolding. In contact with gabbro.
Kg3	64VII07	788560	3168619	bt granite	Allotriomorphic granular; medium grained; acces op, tur, ap; secondary minerals ser, chl; pl with normal zoning replaced by wm+ab; qtz with lobate grain boundaries and square subgrains; common myrmekitic intergrowths within kfs; bt replaced by chl.	Felsic dike, ~20m-thick. Medium to coarse-grained, including segregation felsic bands and pegmatitic phases with grt+qtz+kfs.
Jt	17XII07	791128	3165515	bt-hbl tonalite	Porphyroclastic; medium-fine grained; acces op, zr; pl moderately kaolinitized, discontinuously zoned; qtz as fine-grained recrystallized aggregates; bt defining S-C structures; green hbl delineating folia with fish-like geometries or boudinaged. QAP=35:0:65	Medium-grained, intensively deformed, biotite-hornblende tonalite including cm-scale quartz-rich screens in vertical position. Both tonalite and screens show evident deformational lineation.
Jv	NR-24	789715	3170040	volcani-clastic breccia	Fine to- medium-grained feldspar-quartz fragmented porphyroclasts moderately kaolinitized, discontinuously zoned; it is included cm-scale glomerocrysts of pl+qtz+mc(bt,chl,ms) +cal+op, oriented and elongated in the foliation direction. Embedded in a very fine-grained, pl+qtz matrix. P:M=15:85.	Gray-colored protomylonite with qtz+bt-rich matrix. It has abundant, subrounded, pink, fld phenocrysts, and elongated fragments of greenschists, mafic schists and granitoids. It is cut by younger qtz dikes in oblique sense relative to main attitude and internal fabrics.

Note. ol: olivine; opx: orthopyroxene; cpx: clinopyroxene; lab: labradorite; and: andesine; olg: oligoclase; pl: plagioclase; hbl: hornblende; bt: biotite; op: opaques; zr: zircon; ap: apatite; qtz: quartz; kfs: potassic feldspar; ab: albite; wm: white mica; ep: epidote; tur: tourmaline; hy: hypersthene; aug: augite; sph: titanite. P:M: porphyroclast:matrix ratio; QAP: normalized modal percentages of quartz, alkali feldspar and plagioclase from thin section; PCO: normalized modal percentages of plagioclase, clinopyroxene and orthopyroxene from thin section; PP: normalized modal percentages of plagioclase and pyroxenes from thin section.

by low olivine (0.2–1.9 %) and high hypersthene content (21.9–23.9 %). Chondrite-normalized REE abundances of diorite (Figure 8a) have 7 to 17 times the chondrite level. Our available REE data indicate a minor LREE fractionation (La/Sm_{CN} 1.3–1.7), and suggest a positive Eu anomaly (Figure 8a).

According to the Ti/V ratios of gabbro (Kgb; 7.6–13.3) and diorite (Kd; 16.4 – 20.1), these units plot in the lower limit or within the arc field on the Shervais (1982) Ti-V discrimination diagram (Figure 9).

Felsic units

According to the classification scheme for granitic rocks based in the Fe* *vs* weight per cent SiO_2 diagram ($Fe^*=FeO^t/(FeO^t + MgO)$; Frost *et al.*, 2001), tonalites of the Kt unit (samples NR16 and 12III06) and the Kg1 dike represented by the sample 19VII06 are magnesian. The rest of the felsic samples plot in the ferroan field. Even though, all the felsic units are inside the Cordilleran granites field (Figure 10a). From the MALI diagram (modified alkali-lime index; Frost *et al.*, 2001), Kt and Kg1 units plot in the calcic field, which typify the granitoids of the Cordilleran Mesozoic batholiths. The only exception is sample 41XI08 from Kg2 unit, which is alkaline granite (Figure 10b). In relation to the Shand aluminum saturation index (Al / [Na+K] *vs* Al / [Ca+Na+K]; Terra Softa, Inc., 2009), both the Kt unit and the Kg1 dike 19VII06 plot within the metaluminous field. The other three samples are peraluminous, whereas granite 41XI08 is located in the border of the metaluminous and the peralkaline fields (Figure 10c).

Chondrite-normalized REE abundances of the Kt unit samples (NR16 and 12III06 in Figure 8b) have about 27 times the chondritic levels (except for La of sample 12III06). The REE pattern of sample NR16 from the massive outcrop displays only slight LREE fractionation (La/Sm_{CN} 1.3), a moderate negative Eu anomaly (Eu/Eu* -0.74), and a flat

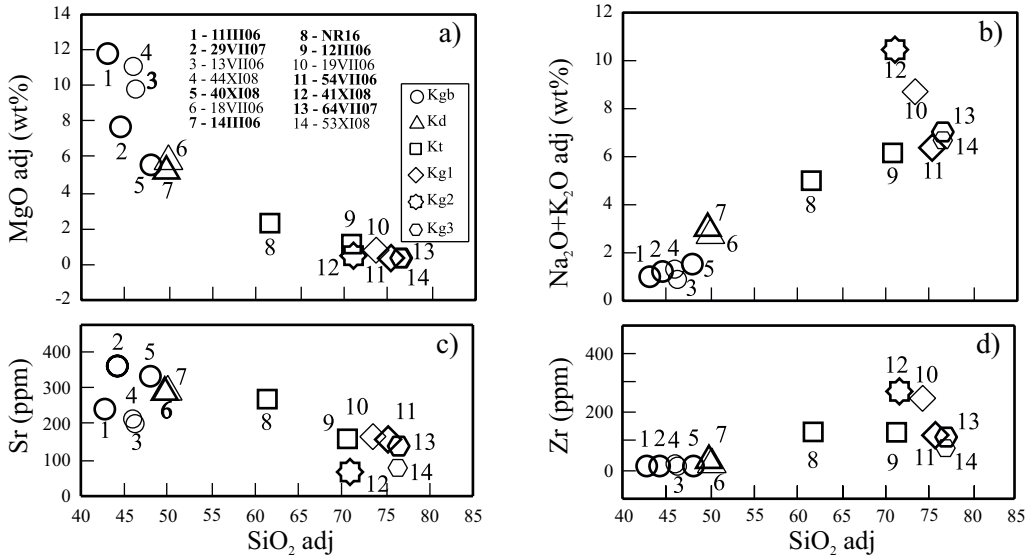

Figure 7. Harker diagrams of MgO (a), alkalis (b), Sr (c) and Zr (d) from the intrusive units. The bolded symbols correspond to samples from the southern part of the suite and unbolded are from the northern part of the suite. adj: adjusted to anhydrous basis.

HREE pattern (Figure 8b). The 12III06 Kt dike shows a similar chondrite-normalized REE pattern and higher LREE fractionaiton (La/Sm_{CN} 2.6) relative to NR16. Available data also suggest a moderate negative Eu anomaly.

Chondrite-normalized REE abundances of the two samples representing the Kg1 unit (12III06 and 19VII06; Figure 8b) are 30 to 45 times the chondritic levels, with a moderate fractionation of LREE (La/Sm_{CN} 2.4–4.8). In turn, the sample 41XI08 (Figure 8b) has about 30 times the chondritic content, slight fractionation of LREE (La/Sm_{CN} 1.6), slight negative Eu anomaly (Eu/Eu* -0.75), and a relative flat HREE pattern (Figure 8b). Finally, the Kg3 unit (samples 64VII07 and 53XI08; Figure 8b) have 10 to 45 times the chondritic content, the highest silica (76.7 wt %) and the lowest magnesium content (0.2–0.3 wt %). In turn, sample 53XI08 shows a highly fractionated LREE (La/Sm_{CN} 3.9-4.8). It is characterized by the absence of a Eu anomaly, a concave-down shape of their HREE with the lowest value at Dy, and a positive slope in their LREE (Figure 8b).

U-Pb GEOCHRONOLOGY

Analytical procedures

Zircons were separated by standard procedures at the Geology Department, CICESE. Crushed, milled, and sieved samples were processed using a Wilfley® table, a Frantz® isodynamic separator, and heavy liquid techniques using methylene iodide. Finally, inclusions-free crystals were selected by handpicking.

Individual zircon crystals were analyzed at the Geosciences Department of the University of Arizona, Tucson, with a Micromass Isoprobe multi-collector ICPMS, equipped with nine Faraday collectors, an axial Daly detector, and four ion-counting channels. An ArF Excimer laser system with an emission wavelength of 193 nm is coupled to the isoprobe. The collector configuration allows measurement of ^{204}Pb with an ion-counting channel whereas ^{206}Pb, ^{207}Pb, ^{208}Pb, ^{232}Th and ^{238}U are measured simultaneously with Faraday detectors. The analyses were conducted following the method described by Gehrels *et al.* (2006) in static mode with a laser beam diameter of 35 µm with output energy of ~32 mJ and a repetition rate of 8 Hz. Each analysis consisted of one 20 seconds-integration on peaks with no laser firing for background measurement and 12 one-second integrations on peaks with laser firing. The background values are used to remove any Hg contribution to the ^{204}Pb mass. Uranium and Thorium concentrations were monitored by analyzing a standard (NIST 610 Glass) with ~500 ppm Th and U, for every sample. Inter-element fractionation was monitored by analyzing zircon standard fragments from Sri Lanka (SL-1) with a known concordant ID-TIMS age of 564 ± 4 Ma (2σ) (Gehrels *et al.*, 2008), once for every four unknown sample zircon grains.

All reported ages are based on the $^{206}Pb/^{238}U$ ratios because errors of the $^{207}Pb/^{235}U$ and $^{206}Pb/^{207}Pb$ ratios are greater due to the low ^{207}Pb signal of young samples. The $^{206}Pb/^{238}U$ ratios were corrected for common lead by using the measured ^{204}Pb assuming an initial Pb composition from Stacey and Kramers (1975) and an uncertainty of 1.0 for $^{206}Pb/^{204}Pb$.

Weighted average ages were calculated using Isoplot v. 3 (Ludwig, 2003). Systematic errors were propagated separately, and include the age of the standard, calibration correction from standard analyses, composition of common Pb, and U decay constant uncertainties. All age uncertainties

Table 2. Representative whole-rock geochemical data, and CIPW-normative minerals of selected samples of gabbroic (Kgb), dioritic (Kd), tonalitic (Kt), and granitic (Kg1, Kg2 and Kg3) units.

Intrusive unit	**Kgb**	**Kgb**	**Kgb**	**Kgb**	**Kgb**	**Kd**	**Kd**
Sample	**44-XI-08**	**13-VII-06**	**40-XI-08**	**11-III-06**	**29-VII-07**	**18-VII-06**	**14-III-06**
UTM coordinates northing/easting	789936/ 3169234	790149/ 3167463	786155/ 3173298	788533/ 3170048	786701/ 3171684	788831/ 3167304	788161/ 3168018
Analytical code	4Litho	4B	4Litho	4B	4B	4B	4B
(a) Major elements (wt %)							
SiO_2	45.35	45.82	47.50	42.86	44.29	50.17	49.27
TiO_2	0.20	0.44	0.20	0.65	0.34	0.97	1.16
Al_2O_3	19.81	17.17	23.66	17.82	23.49	18.42	18.18
$Fe_2O_3^t$	6.05	11.20	5.92	14.18	9.46	12.50	12.97
MnO	0.12	0.23	0.15	0.20	0.13	0.22	0.24
MgO	9.45	10.93	5.48	11.62	7.66	5.76	5.24
CaO	16.27	13.10	14.73	12.50	13.81	10.20	9.44
Na_2O	0.81	1.10	1.26	0.99	1.20	2.74	2.76
K_2O	0.03	0.11	0.21	0.01	0.01	0.01	0.41
P_2O_5	0.02	0.03	0.02	0.01	0.01	0.10	0.18
LOI	0.56	-0.05	1.19	-0.37	-0.22	-0.45	0.30
Total	98.67	100.10	100.30	100.50	100.10	100.60	100.20
(b) CIPW norms (wt %)							
Q	0.00	0.00	0.00	0.00	0.00	0.00	0.00
Or	0.18	0.66	1.26	0.03	0.03	0.03	2.45
Ab	7.02	9.38	10.81	7.01	10.20	23.18	23.65
An	51.56	41.93	59.09	44.35	58.96	37.94	36.46
Ne	0.00	0.00	0.00	0.76	0.00	0.00	0.00
C	0.00	0.00	0.00	0.00	0.00	0.00	0.00
Di	24.83	18.96	12.07	14.56	8.00	9.94	8.13
Hy	0.75	8.03	13.52	0.00	0.81	23.90	21.86
Ol	13.85	17.64	1.49	29.56	19.71	0.18	1.90
Mt	1.37	2.50	1.33	2.45	1.64	2.76	2.90
Il	0.39	0.83	0.39	1.25	0.64	1.85	2.22
Ap	0.05	0.07	0.05	0.02	0.02	0.23	0.42
Mg#	78.50	69.52	68.39	64.82	64.55	51.85	48.57
(c) Trace elements (ppm)							
Ba	17.0	48.0	72.0	17.0	24.0	75.0	121.0
Rb	-	-	4.0	-	-	-	-
Sr	198.0	211.0	331.0	235.0	357.0	288.0	290.0
Zr	8.0	17.0	7.0	4.0	3.0	16.0	40.0
Y	2.0	5.0	5.0	1.0	-	14.0	16.0
Nb	-	-	1.0	-	-	-	-
Th	0.3	-	1.0	-	-	-	-
Pb	-	8.0	-	-	-	-	-
Ga	12.0	-	15.0	-	-	-	-
Zn	30.0	113.0	-	70.0	47.0	91.0	91.0
Cu	20.0	57.0	-	116.0	11.0	108.0	57.0
Cr	610.0	369.0	190.0	165.0	191.0	152.0	148.0
Ni	70.0	46.0	-	71.0	41.0	20.0	11.0
V	118.0	198.0	157.0	414.0	241.0	355.0	346.0
Hf	0.3	-	0.5	-	-	1.0	0.9
Cs	-	-	-	-	-	-	-
Sc	44.0	47.3	26.0	42.3	21.7	41.0	40.8
Ta	-	-	0.4	-	<1.0	-	-
Co	36.0	64.0	17.0	74.0	48.0	41.0	34.0
U	-	-	0.1	-	-	-	-
(d) Rare earth elements (ppm)							
La	0.90	1.50	1.50	0.50	0.60	3.10	5.40
Ce	1.00	4.00	5.80	-	-	7.00	10.00
Pr	0.18	-	0.83	-	-	-	-
Nd	1.10	-	3.60	-	-	-	10.00

continues

Table 2 (continued). Representative whole-rock geochemical data, and CIPW-normative minerals of selected samples of gabbroic (Kgb), dioritic (Kd), tonalitic (Kt), and granitic (Kg1, Kg2 and Kg3) units.

Intrusive unit	**Kgb**	**Kgb**	**Kgb**	**Kgb**	**Kgb**	**Kd**	**Kd**
Sample	**44-XI-08**	**13-VII-06**	**40-XI-08**	**11-III-06**	**29-VII-07**	**18-VII-06**	**14-III-06**
UTM coordinates northing/easting	789936/ 3169234	790149/ 3167463	786155/ 3173298	788533/ 3170048	786701/ 3171684	788831/ 3167304	788161/ 3168018
Analytical code	4Litho	4B	4Litho	4B	4B	4B	4B
(d, continued) Rare earth elements (ppm)							
Sm	0.40	0.80	1.00	0.40	0.30	1.50	2.00
Eu	0.24	0.50	0.53	0.40	0.30	0.90	1.20
Gd	0.60	-	1.20	-	-	-	-
Tb	0.10	-	0.20	-	-	-	-
Dy	0.70	-	1.30	-	-	-	-
Ho	0.20	-	0.30	-	-	-	-
Er	0.40	-	0.70	-	-	-	-
Tm	0.06	-	0.11	-	-	-	-
Yb	0.40	1.20	0.70	0.60	0.30	2.20	2.40
Lu	0.06	0.16	0.11	-	-	0.35	0.34
Intrusive unit	**Kt**	**Kt**	**Kg1**	**Kg1**	**Kg2**	**Kg3**	**Kg3**
Sample	**NR16**	**12-III-06**	**54-VII-06**	**19-VII-06**	**41-XI-08**	**64-VII-07**	**53-XI-08**
UTM coordinates northing/easting	787703/ 3167821	788257/ 3169820	786790/ 3170483	788929/ 3167138	788761/ 3171263	788560/ 3168619	788854/ 3168494
Analytical code	4Litho	4B	4B	4B	4Litho	4B	4Litho
(a) Major elements (wt %)							
SiO_2	60.01	70.07	74.53	73.84	69.92	75.89	75.53
TiO_2	0.62	0.32	0.12	0.34	0.38	0.08	0.11
Al_2O_3	16.46	14.29	13.16	13.23	13.45	12.30	12.60
$Fe_2O_3^t$	7.39	4.03	2.66	2.84	2.26	2.32	1.71
MnO	0.16	0.07	0.03	0.04	0.06	0.06	0.06
MgO	2.24	1.00	0.31	0.67	0.45	0.20	0.25
CaO	5.94	3.12	1.91	2.47	1.35	1.18	1.68
Na_2O	3.96	3.60	3.82	3.13	3.31	3.69	3.92
K_2O	1.00	2.52	2.47	3.62	7.10	3.38	2.72
P_2O_5	0.17	0.08	0.03	0.08	0.09	0.03	0.04
LOI	0.45	0.34	0.34	0.44	0.17	0.18	0.40
Total	98.38	99.45	99.39	100.70	98.56	99.31	99.01
(b) CIPWnorms (wt %)							
Q	15.63	39.66	37.82	34.85	21.02	38.22	38.37
Or	6.07	12.45	14.76	21.38	42.72	20.18	16.32
Ab	34.41	38.58	32.70	26.47	28.52	31.55	33.68
An	24.83	4.18	9.39	11.35	0.89	5.72	8.20
Ne	0.00	0.00	0.00	0.00	0.00	0.00	0.00
C	0.00	0.10	0.81	0.00	0.00	0.50	0.25
Di	3.58	0.00	0.00	0.31	4.45	0.00	0.00
Hy	11.24	2.77	3.01	3.54	0.42	2.56	2.09
Ol	0.00	0.00	0.00	0.00	0.00	0.00	0.00
Mt	2.63	1.44	1.21	1.28	1.04	1.05	0.78
Il	1.20	0.67	0.24	0.64	0.74	0.15	0.21
Ap	0.40	0.16	0.07	0.19	0.21	0.07	0.10
Mg#	44.12	14.75	25.10	40.41	36.38	19.84	29.60
(c) Trace elements (ppm)							
Ba	231.0	557.0	596.0	759.0	598.0	536.0	491.0
Rb	19.0	80.0	80.0	110.0	89.0	60.0	64.0
Sr	264.0	152.0	155.0	161.0	63.0	80.0	135.0
Zr	119.0	117.0	108.0	228.0	250.0	69.0	102.0
Y	30.0	25.0	9.0	20.0	27.0	17.0	11.0
Nb	2.0	-	-	-	5.0	-	2.0
Th	1.7	7.3	11.7	11.7	4.6	17.6	7.2

continues

Table 2 (continued). Representative whole-rock geochemical data, and CIPW-normative minerals of selected samples of gabbroic (Kgb), dioritic (Kd), tonalitic (Kt), and granitic (Kg1, Kg2 and Kg3) units.

Intrusive unit	**Kt**	**Kt**	**Kg1**	**Kg1**	**Kg2**	**Kg3**	**Kg3**
Sample	**NR16**	**12-III-06**	**54-VII-06**	**19-VII-06**	**41-XI-08**	**64-VII-07**	**53-XI-08**
UTM coordinates northing/easting	787703/ 3167821	788257/ 3169820	786790/ 3170483	788929/ 3167138	788761/ 3171263	788560/ 3168619	788854/ 3168494
Analytical code	4Litho	4B	4B	4B	4Litho	4B	4Litho
(c) Trace elements (ppm)							
Pb	-	-	7.0	6.0	-	9.0	-
Ga	19.0	-	-	-	12.0	-	12.0
Zn	80.0	44.0	17.0	41.0	-	25.0	-
Cu	30.0	8.0	23.0	16.0	10.0	23.0	-
Cr	210.0	311.0	299.0	18.0	210.0	328.0	280.0
Ni	-	22.0	89.0	44.0	-	91.0	-
V	103.0	50.0	5.0	52.0	18.0	-	7.0
Hf	3.1	3.7	3.2	7.3	6.0	2.9	2.8
Cs	0.5	-	-	3.0	-	3.4	1.4
Sc	21.0	12.9	2.1	7.5	13.0	2.6	2.0
Ta	0.2	-	-	-	0.5	-	0.3
Co	13.0	6.0	3.0	7.0	3.0	-	2.0
U	0.5	-	1.4	2.1	1.5	2.8	1.1
(d) Rare earth elements (ppm)							
La	8.80	11.70	14.70	10.30	12.50	16.40	12.10
Ce	19.50	18.00	24.00	19.00	31.00	23.00	22.40
Pr	2.75	-	-	-	4.16	-	2.50
Nd	13.90	9.00	6.00	-	18.40	15.00	9.10
Sm	4.10	2.80	1.90	2.70	4.70	2.10	1.90
Eu	1.18	0.90	0.80	1.00	1.16	-	0.52
Gd	4.90	-	-	-	4.70	-	1.80
Tb	0.90	-	-	-	0.80	-	0.30
Dy	5.40	-	-	-	4.60	-	1.80
Ho	1.20	-	-	-	1.00	-	0.40
Er	3.60	-	-	-	3.20	-	1.30
Tm	0.56	-	-	-	0.52	-	0.21
Yb	3.50	3.90	1.90	2.60	3.40	2.80	1.50
Lu	0.50	0.60	0.30	0.40	0.52	0.38	0.26

Note: Sampling does not include cumulate components from gabbro, intrusive enclaves, host rock screens, and late-stage veins from felsic bodies. Major and trace element compositions analyzed under 4Litho code, and major element compositions analyzed under 4B, were determined using lithium metaborate/tetraborate fusion ICP. Trace elemental compositions analyzed under 4B code were determined using total digestion ICP (Cu, Mo, Ni, S, Zn), lithium metaborate/tetraborate fusion ICP (Sr, V, Y, Zr), and instrumental neutron activation technique (As, Co, Cr, Hf, Rb, Sc, Th, U, La, Ce, Nd, Sm, Eu, Yb, Lu). Because the two techniques used (4Litho and 4B codes) and their different limit of detection, trace element compositions analyzed under 4B code should be treated with caution. CIPW norms are on an anhydrous 100% adjusted basis and using Fe_2O_3/FeO ratio after Middlemost (1989), using the SINCLAS computer program (Verma *et al.*, 2003). Fe2O3^T: total iron expressed as Fe_2O_3; Mg#: 100 $Mg^{2+}/(Mg^{2+} + Fe^{2+})$, atomic; FeO^T: total iron expressed as FeO; dashes indicate those elements that was not analysed. All the analyses were commercially made at the Actlabs laboratories.

are reported at the 2-sigma level (2σ). U-Pb geochronological data are presented in Table 3.

Zircon U-Pb results

We analyzed zircons from a hosting granitoid rock of the unit Jt (sample 17XII07; Figure 2), a hosting volcanic breccia of the Jv unit (sample NR24), and a tonalite from the Kt massive body (sample NR16). Measurements were made at the center and tips of the zircon crystals. Zircons from all three samples are colorless, and have a well-developed prism {110} and pyramid {101} forms. They also have U/Th <3 indicating a magmatic origin (Rubatto, 2002).

Zircons from the plutonic rocks (17XII07 and NR16) are dominantly prismatic (length-to-width ratio between 2 and 4). Separated grain sizes vary from 100 to 450 µm. Thirty one zircon grains from sample 17XII07 were measured, yielding a weighted $^{206}Pb/^{238}U$ age of 151.6 ± 2.6 Ma (2σ, including systematic error; Figure 11a). Thirty two laser spots were measured on zircons from sample NR16. They yield a weighted $^{206}Pb/^{238}U$ age of 108.4 ± 2.2 Ma (2σ, including systematic error; Figure 11b). Zircon crystals from sample NR24 are long prismatic (l/w of 6 to12), ranging from 550 to 120 µm in size. Twenty six laser spots on zircons from sample NR24 yield a weighted $^{206}Pb/^{238}U$ age of 139.5 ± 2.0 Ma (2σ, including systematic error; Figure 11c). In one grain of the last sample an inherited zircon core with a

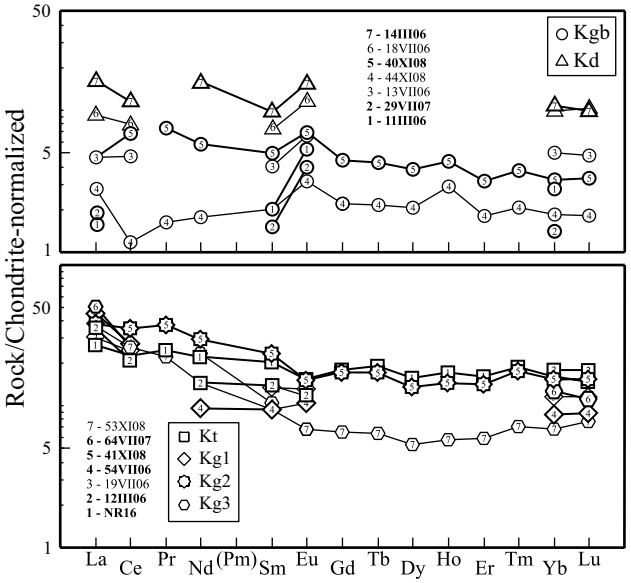

Figure 8. Chondrite-normalized Rare Earth Elements (REE) patterns of (a) gabbro (Kgb) and diorite (Kd), and (b) tonalite (Kt), biotite-rich tonalite-granite (Kg1), hornblende-rich granite-syenogranite (Kg2) and biotite granites (Kg3). The bolded symbols correspond to samples from the southern part of the suite and unbolded are from the northern part of the suite. Incomplete geochemical data on samples 11III06, 29VI07, 13VII06, 18VII06, 12III06, 19VII06, 54VII06 and 64VII07 is due to their composition determination by instrumental neutron activation technique. The reference values are from Nakamura (1974) and Haskin *et al.* (1968).

$^{206}Pb/^{238}U$ age of 152.7 ± 1.5 Ma (1σ analytical uncertainty) was detected.

DISCUSSION

Host rocks

The host rocks of the Nuevo Rosarito plutonic suite are dominated by volcanic units and granitoid rocks. The granitoids have minor screens of volcanics, amphibolite and clastic sedimentary rocks. Accordingly, we assume that the Nuevo Rosarito plutonic suite was emplaced into a volcano-plutonic assemblage.

In the southern part of the suite, the 151.6 ± 2.6 Ma U-Pb age obtained from the granitoid Jt unit makes this plutonic sequence contemporaneous to the San Andrés volcano-plutonic complex (locality 11; Figure 1a), whose U-Pb zircon ages vary between 134.5 and 155.6 Ma (Kimbrough and Moore, 2003). In the northern part of the suite, the dated sample NR24 from a volcanic breccia deposit yield an U-Pb zircon age of 139.5 ± 2.0 Ma, which is also contemporaneous to the San Andrés volcano-plutonic complex and to the volcanogenic deposits from the Eugenia formation. The orientations of the fabrics of all host rock units (including the screens within the gabbroic rocks) are persistent at the regional scale, except for the outcrops close to the margins of the southern part of the suite, where fabrics have a tendency to outline its circular geometry. Such tendency indicates that ductile deformation and overturning of the structures occurred before the emplacement of the gabbro.

Mafic units (Kgb, Kd, Kqd)

The absence of olivine and the presence of orthopyroxene in the gabbroic (Kgb) and dioritic (Kd) rocks allow us to compare the mafic units with the amphibole-orthopyroxene subseries of the gabbroic rocks of the Peninsular Ranges batholith in southern California (Walawender and Smith, 1980). The Kgb rocks have alumina concentrations in the range of 17.2 to 23.7% (Table 2), exceeding the normal content for sub-alkaline gabbroic rocks (Cox *et al.*, 1979). Such high alumina content is a typical composition of high-alumina arc basalts (17–22 wt %; *e.g.*, Fournelle and Marsh, 1991), which is the dominant rock type in most island arc settings (*e.g.*, Wilson, 1989). As observed elsewhere (Fournelle and Marsh, 1991; Tate *et al.*, 1999), positive Eu anomaly (Figure 8a) is associated with the presence of the plagioclase cumulates from the southern part of the suite (Figure 4a).

The Kd interfingered bodies (Figure 4d) exhibit at the microscopic and hand specimen scales a clear interlocking texture (Figure 6a). According to Hibbard and Waters (1985), such texture suggests magmatic fracturing with presence of intergranular melt that, in this case, is dioritic. Non-fractured fragments of gabbro included within diorite dikes support a late stage magmatic fracturing with a minor presence of intergranular dioritic melt compared with the interfingered bodies. Both the Kd interfingered bodies and Kd dikes do not have chilled margins, suggesting a small temperature contrast between the dioritic melt and the hosting gabbro. As a result, the textural variation in the Kd dikes and the fact that diorite is enclosed by the gabbro also suggest that dioritic melt was segregated from a gabbroic mush. This interpretation is supported by the following geochemical data: (a) the MgO and alkalis contents of

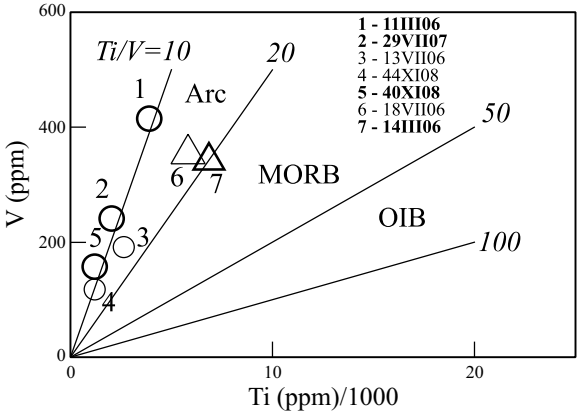

Figure 9. Ti-V discrimination diagram for basalts (Shervais, 1982) applied to Nuevo Rosarito plutonic suite.

the two diorite samples (18VII06 and 14III06) are similar to the lowest compositional values of the same oxides of the gabbroic rocks (Figures 7a and 7b); (b) dioritic and gabbroic rocks have comparable REE patterns with positive Eu anomalies (Figure 8a); (c) diorite has higher REE abundances and higher incompatible element concentrations (*e.g.* Ba, Y, Zr, Hf, La, Ce; Table 2) than gabbro.

Decades of observations of intrusive geometries have shown that the alignment of magmatic bodies is the product of (a) melt channelizing through preexisting fabric anisotropies (*e.g.*, Sawyer, 2001) or (b) melt migration along extensional fractures or dilatant structures generated by active stress regimes (*e.g.*, Anderson, 1938, 1951; D'Lemos *et al.*, 1992; Brown and Solar, 1998; Barros *et al.*, 2001; Geshi, 2001). In accordance with previous studies, we favor the generation of extensional structures oriented NNE-SSW in a progressively crystallizing gabbroic mass as the mechanism responsible for the dioritic emplacement because (a) it is unexpected for a progressively crystallizing magmatic body to hold any preexisting anisotropy; (b) the Kd interfingered bodies and Kd dikes have a persistent orientation within the gabbro (Figure 3d); (c) the vertical geometry of the dioritic bodies suggest a vertical direction of the maximum main stress; and (d) the lack of field evidence for any transpressional or transtensional deformation to produce dilatant structures (*e.g.*, en-echelon structures, structures with systematic orientation variation, etc.) during the diorite emplacement.

This proposal may be regionally reconciled with the numerous mafic dikes oriented NNE-SSW reported by Busby *et al.* (2006) near El Rosario (Figure 1a; locality 6), which were interpreted by these authors from field observations and U-Pb in zircon data as syn-volcanic faults generated under an extensional regime at *ca.* 111 Ma.

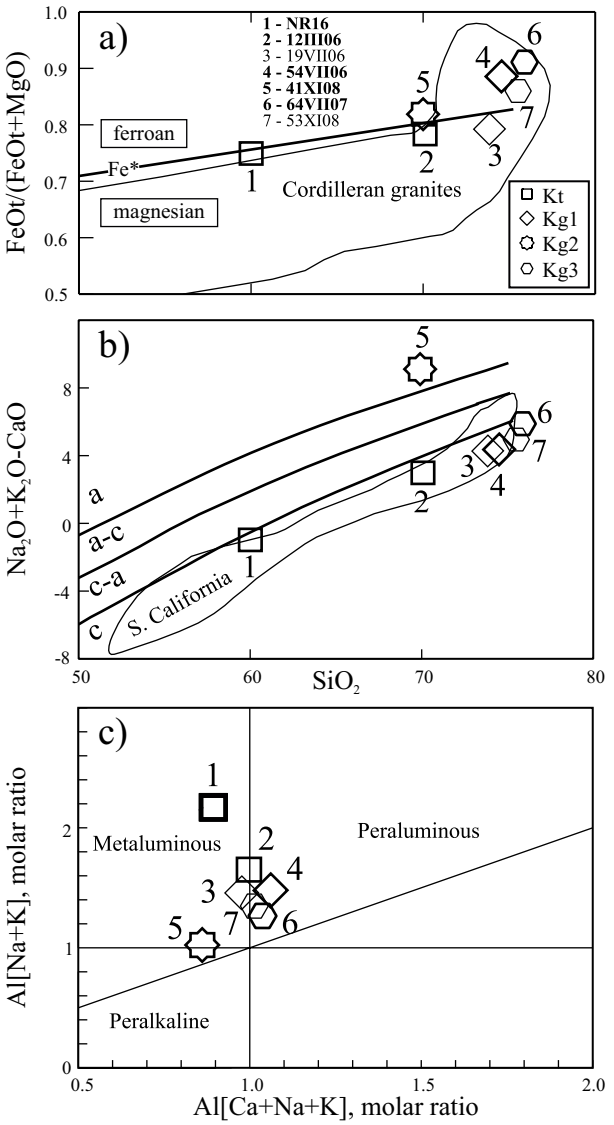

Figure 10. Geochemical classification diagrams of granitic rocks after Frost *et al.* (2001). The bolded symbols correspond to samples from the southern part of the suite and unbolded are from the northern part of the suite. Samples are listed within the diagrams. (a) $FeO^t/(FeO^t + MgO)$ *vs.* SiO_2 (wt%) diagram indicating the ferroan and magnesian fields, and the composition range of the Cordilleran granites. (b) Na_2O+K_2O-CaO *vs.* SiO_2 (wt%) diagram showing the composition range of the calcic southern California batholith. Abbreviations: c: calcic; c-a: calc-alkalic; a-c: alkali-calcic; a: alkalic. (c) Shand's aluminum saturation diagram.

Felsic units (Kt, Kg1, Kg2 and Kg3)

The geochemistry of the felsic units of the Nuevo Rosarito plutonic suite (Figures 10a and 10b) is consistent with the composition of the Cordilleran batholiths reported by Frost *et al.* (2001), except for the Kg2 dike, which shows anomalously high alkalis (sample 41XI08; Figure 10b). Nevertheless, chondrite-normalized REE patterns of this sample, as well as those of the rest of the felsic units, are consistent with those reported by Gromet and Silver (1987) for the western zone of the Peninsular Ranges batholith. Also, the Sr content, and the Sm/Dy and Sr/Y ratios of all the felsic units can be compared with those reported by Gromet and Silver (1987) and Tulloch and Kimbrough (2003) for the western zone batholith.

The REE pattern of the Kg3 unit is distinct from the rest of the felsic units, specifically the concave shape pattern of their HREE which is indicative of hornblende fractionation (Gromet and Silver, 1987; Bea, 1996).

Syn-emplacement deformation

The conspicuous intense solid-state fabrics exhibited by the Kt dikes and the Kg1 and Kg2 bodies at the mesoscale (Figures 4e), and the ductile deformation that the gabbro usually shows in the vicinity of the felsic dikes (Figures 4h and 4i), strongly suggest that the ductile deformation in these units was simultaneous to their emplacement. Evidence of syn-emplacement deformation is also found at the microscale through the submagmatic fractures (Bouchez *et al.*, 1992; Park and Means, 1996) observed within the feldspar grains of many Kt and Kg1 unit samples, as well

Table 3. U-Pb zircon geochronologic analyses by Laser-Ablation Multicollector ICP Mass Spectrometer.

Sample	U (ppm)	$^{206}Pb/^{204}Pb$	U/Th	Isotopic ratios					Apparent ages (Ma)						Best age (Ma)	± (Ma)
				$^{207}Pb^*/^{235}U$	± (%)	$^{206}Pb^*/^{238}U$	± (%)	error corr.	$^{206}Pb^*/^{238}U$	± (Ma)	$^{207}Pb^*/^{235}U$	± (Ma)	$^{206}Pb^*/^{207}Pb^*$	± (Ma)		
NR16																
01T	60	190	2.8	0.13320	21.8	0.01693	12.2	0.56	108.2	13.1	127.0	26.0	493.8	401.1	108.2	13.1
02T	78	227	2.5	0.15532	13.3	0.01663	9.7	0.73	106.3	10.2	146.6	18.1	861.1	188.4	106.3	10.2
03T	177	439	2.3	0.11973	7.6	0.01650	4.6	0.60	105.5	4.8	114.8	8.2	312.9	137.4	105.5	4.8
04T	57	243	3.0	0.16793	14.0	0.01637	3.8	0.27	104.7	3.9	157.6	20.4	1052.3	272.2	104.7	3.9
05T	98	264	3.5	0.12375	15.5	0.01636	5.3	0.34	104.6	5.5	118.5	17.4	407.1	328.4	104.6	5.5
06T	76	237	2.5	0.12458	18.8	0.01667	6.3	0.34	106.6	6.7	119.2	21.1	379.2	400.6	106.6	6.7
07T	74	266	2.3	0.14827	18.9	0.01663	6.2	0.33	106.3	6.5	140.4	24.8	763.4	379.6	106.3	6.5
08T	92	268	2.1	0.12843	15.1	0.01709	4.2	0.28	109.2	4.6	122.7	17.4	392.4	325.8	109.2	4.6
09T	76	224	4.6	0.12798	19.0	0.01729	5.4	0.28	110.5	5.9	122.3	21.9	358.0	415.1	110.5	5.9
10T	97	295	2.5	0.12135	17.4	0.01725	5.0	0.29	110.3	5.5	116.3	19.1	241.2	386.8	110.3	5.5
11T	159	456	4.2	0.11738	13.7	0.01699	4.1	0.30	108.6	4.4	112.7	14.6	200.4	303.7	108.6	4.4
12T	113	387	1.9	0.15511	16.9	0.01701	7.7	0.46	108.7	8.3	146.4	23.0	810.7	315.9	108.7	8.3
13T	575	1821	1.4	0.14945	12.2	0.01724	4.9	0.40	110.2	5.3	141.4	16.1	704.4	238.5	110.2	5.3
14T	98	312	2.8	0.12948	13.0	0.01685	6.7	0.52	107.7	7.1	123.6	15.1	441.5	247.8	107.7	7.1
15T	348	989	1.5	0.14455	8.8	0.01755	1.8	0.21	112.1	2.0	137.1	11.3	594.4	186.2	112.1	2.0
16C	227	637	2.4	0.13058	13.4	0.01667	4.1	0.31	106.6	4.4	124.6	15.8	484.3	283.4	106.6	4.4
17C	135	441	2.3	0.12354	10.2	0.01735	3.7	0.36	110.9	4.0	118.3	11.3	269.8	217.6	110.9	4.0
18C	132	357	2.3	0.12068	10.9	0.01639	3.9	0.36	104.8	4.1	115.7	12.0	345.5	231.4	104.8	4.1
19C	202	516	2.2	0.11635	10.1	0.01651	5.0	0.49	105.5	5.3	111.8	10.7	246.4	203.2	105.5	5.3
20C	91	274	2.6	0.12614	16.0	0.01675	3.2	0.20	107.1	3.4	120.6	18.2	397.2	354.2	107.1	3.4
21C	53	252	3.7	0.15921	15.2	0.01659	6.1	0.40	106.0	6.5	150.0	21.2	917.2	287.5	106.0	6.5
22	181	534	3.2	0.11649	15.5	0.01694	3.8	0.24	108.3	4.0	111.9	16.4	188.9	352.1	108.3	4.0
23	99	281	2.5	0.11278	19.8	0.01613	8.9	0.45	103.1	9.1	108.5	20.3	227.9	410.6	103.1	9.1
24	119	374	2.8	0.11460	14.5	0.01641	5.5	0.38	104.9	5.7	110.2	15.1	224.7	311.2	104.9	5.7
25	223	710	2.4	0.11272	13.1	0.01698	7.1	0.54	108.5	7.6	108.4	13.5	106.4	260.6	108.5	7.6
26	93	298	2.3	0.11541	23.2	0.01716	5.4	0.23	109.7	5.9	110.9	24.4	136.7	535.1	109.7	5.9
27	83	239	2.2	0.11780	19.9	0.01653	7.3	0.36	105.7	7.6	113.1	21.3	271.4	428.9	105.7	7.6
28	135	413	2.1	0.12756	9.5	0.01755	4.8	0.50	112.2	5.3	121.9	11.0	316.5	187.7	112.2	5.3
29	90	297	3.4	0.12058	18.1	0.01656	8.3	0.46	105.9	8.7	115.6	19.8	320.9	367.8	105.9	8.7
30	87	294	2.6	0.13771	19.4	0.01663	8.6	0.44	106.3	9.1	131.0	23.8	605.3	377.9	106.3	9.1
31	98	322	3.6	0.12438	16.8	0.01757	7.1	0.42	112.3	7.9	119.0	18.9	256.4	352.3	112.3	7.9
32	109	388	2.8	0.12242	13.4	0.01709	4.7	0.35	109.2	5.1	117.3	14.9	283.3	288.7	109.2	5.1
33	67	277	2.9	0.12930	12.4	0.01692	3.8	0.30	108.2	4.0	123.5	14.4	429.3	263.6	108.2	4.0
34	180	482	2.4	0.11565	10.1	0.01663	2.9	0.29	106.3	3.0	111.1	10.6	215.0	223.4	106.3	3.0
35	161	487	3.8	0.10873	17.2	0.01696	5.6	0.32	108.4	6.0	104.8	17.2	23.5	394.0	108.4	6.0
36	94	266	2.6	0.12664	14.9	0.01664	5.6	0.38	106.4	5.9	121.1	17.0	420.7	309.8	106.4	5.9
37C	531	1601	2.8	0.13829	7.2	0.01823	3.9	0.54	116.4	4.5	131.5	8.9	413.5	135.1	116.4	4.5
38C	96	302	2.2	0.11150	18.3	0.01615	6.2	0.34	103.3	6.4	107.3	18.7	198.0	403.5	103.3	6.4
NR24																
01	993	2426	2.1	0.15576	6.3	0.02217	3.9	0.61	141.3	5.4	147.0	8.6	238.8	115.5	141.3	5.4
02	492	892	1.9	0.14874	7.4	0.02157	3.7	0.50	137.6	5.1	140.8	9.7	195.1	148.5	137.6	5.1
03	485	1121	1.8	0.15519	4.0	0.02185	2.9	0.74	139.3	4.0	146.5	5.4	263.7	61.2	139.3	4.0
04	608	1877	1.3	0.14402	5.9	0.02148	3.6	0.61	137.0	4.9	136.6	7.6	129.6	110.2	137.0	4.9
05	749	1456	1.8	0.14723	5.4	0.02185	2.9	0.53	139.3	4.0	139.5	7.1	141.8	108.3	139.3	4.0
06	2042	5712	1.7	0.16201	2.3	0.02397	1.0	0.45	152.7	1.5	152.5	3.3	148.8	48.2	152.7	1.5
06A	2158	2476	1.7	0.14497	4.8	0.02169	1.5	0.32	138.3	2.1	137.5	6.2	122.7	107.3	138.3	2.1
07	318	1076	1.8	0.15231	5.8	0.02223	3.7	0.65	141.7	5.2	143.9	7.8	180.3	102.9	141.7	5.2
08	1158	2935	3.2	0.14457	4.3	0.02166	2.0	0.47	138.1	2.8	137.1	5.5	119.0	89.8	138.1	2.8
09	692	2212	1.4	0.14752	3.9	0.02174	2.8	0.73	138.6	3.9	139.7	5.1	158.2	63.0	138.6	3.9
10	540	1650	2.0	0.14768	4.7	0.02160	1.3	0.29	137.7	1.8	139.9	6.2	176.1	105.4	137.7	1.8
11	555	1627	1.6	0.14973	5.2	0.02208	1.8	0.35	140.8	2.5	141.7	6.8	156.4	113.0	140.8	2.5
12	1815	5305	1.9	0.14788	3.1	0.02218	1.4	0.45	141.4	2.0	140.0	4.1	116.3	66.0	141.4	2.0
13	347	1200	1.9	0.15118	8.9	0.02248	6.1	0.68	143.3	8.6	143.0	11.9	136.7	153.2	143.3	8.6
14	644	2084	1.3	0.14856	6.2	0.02217	1.7	0.28	141.4	2.4	140.6	8.2	128.1	141.3	141.4	2.4
15	1052	2762	2.2	0.14606	4.8	0.02205	1.5	0.31	140.6	2.1	138.4	6.2	101.1	108.0	140.6	2.1

continues

Table 3 (continued). U-Pb zircon geochronologic analyses by Laser-Ablation Multicollector ICP Mass Spectrometer.

Sample	U (ppm)	$^{206}Pb/^{204}Pb$	U/Th	Isotopic ratios					Apparent ages (Ma)						Best age (Ma)	± (Ma)
				$^{207}Pb^*/^{235}U$	± (%)	$^{206}Pb^*/^{238}U$	± (%)	error corr.	$^{206}Pb^*/^{238}U$	± (Ma)	$^{207}Pb^*/^{235}U$	± (Ma)	$^{206}Pb^*/^{207}Pb^*$	± (Ma)		
NR24 (continued)																
16	1167	4472	3.8	0.14647	3.7	0.02192	1.0	0.27	139.8	1.4	138.8	4.8	121.5	83.7	139.8	1.4
17	477	1516	2.1	0.14966	4.5	0.02196	1.8	0.40	140.0	2.5	141.6	5.9	168.3	95.5	140.0	2.5
18	677	2232	1.6	0.14008	8.1	0.02182	2.8	0.35	139.1	3.9	133.1	10.1	26.9	181.5	139.1	3.9
19	1004	3127	1.8	0.14286	4.7	0.02160	3.1	0.67	137.8	4.3	135.6	6.0	97.1	83.1	137.8	4.3
20	565	1852	1.4	0.14617	4.0	0.02170	1.5	0.36	138.4	2.0	138.5	5.2	141.2	87.6	138.4	2.0
21	422	1770	1.8	0.16237	4.4	0.02171	3.0	0.67	138.4	4.1	152.8	6.3	381.5	73.8	138.4	4.1
22	393	1267	2.4	0.15151	5.5	0.02156	4.7	0.87	137.5	6.5	143.2	7.3	239.4	63.2	137.5	6.5
23	511	2001	3.0	0.14520	4.5	0.02173	2.4	0.53	138.6	3.3	137.7	5.8	121.4	90.1	138.6	3.3
24	433	1511	2.4	0.15071	5.1	0.02192	3.0	0.60	139.8	4.2	142.5	6.7	189.2	94.1	139.8	4.2
25	365	1042	2.5	0.15160	5.7	0.02170	3.8	0.66	138.4	5.2	143.3	7.6	225.5	97.9	138.4	5.2
17XII07																
01	395	10632	2.5	0.1580	3.3	0.0235	1.2	0.36	150.0	1.8	149.0	4.6	132.2	72.6	150.0	1.8
02	451	7691	2.6	0.1626	2.1	0.0236	1.0	0.48	150.2	1.5	153.0	2.9	196.5	42.2	150.2	1.5
03	361	6368	3.6	0.1642	4.5	0.0240	2.6	0.58	152.8	4.0	154.4	6.4	179.4	84.8	152.8	4.0
04	250	2825	2.2	0.1681	3.6	0.0240	1.0	0.28	152.6	1.5	157.8	5.2	236.2	79.6	152.6	1.5
05	373	8945	2.7	0.1585	5.5	0.0240	1.0	0.18	152.7	1.5	149.4	7.6	97.8	127.6	152.7	1.5
06	289	6841	2.4	0.1617	3.1	0.0234	1.0	0.32	149.4	1.5	152.2	4.4	195.9	67.9	149.4	1.5
07	296	5561	3.8	0.1619	3.9	0.0240	1.1	0.27	152.6	1.6	152.3	5.6	148.3	89.0	152.6	1.6
08	370	4022	2.5	0.1625	5.4	0.0235	1.0	0.18	149.7	1.5	152.9	7.7	203.5	124.2	149.7	1.5
09	369	7045	2.4	0.1635	3.3	0.0238	1.0	0.30	151.9	1.5	153.7	4.7	182.7	73.3	151.9	1.5
10	237	4469	1.8	0.1594	4.5	0.0234	3.1	0.68	149.3	4.6	150.1	6.3	163.7	77.2	149.3	4.6
11	266	4541	3.2	0.1593	5.7	0.0236	1.0	0.18	150.4	1.5	150.1	7.9	146.4	131.4	150.4	1.5
12	577	8915	1.9	0.1667	1.7	0.0241	1.0	0.60	153.8	1.5	156.6	2.4	199.3	31.1	153.8	1.5
13	369	6207	2.2	0.1584	4.6	0.0234	3.0	0.65	149.1	4.4	149.3	6.3	151.5	80.9	149.1	4.4
14	939	9591	1.8	0.1659	1.5	0.0240	1.0	0.67	152.8	1.5	155.8	2.1	202.7	25.5	152.8	1.5
15	248	3041	2.3	0.1711	3.0	0.0239	1.9	0.62	152.6	2.8	160.4	4.4	277.8	53.5	152.6	2.8
16	494	7655	2.8	0.1585	4.0	0.0231	1.2	0.31	147.5	1.8	149.4	5.5	179.7	88.0	147.5	1.8
17	230	4553	3.3	0.1598	5.3	0.0235	1.0	0.19	149.5	1.5	150.6	7.4	166.9	121.7	149.5	1.5
18	316	4293	2.1	0.1627	4.0	0.0239	1.0	0.25	152.5	1.5	153.0	5.7	161.9	90.6	152.5	1.5
19	342	8072	2.4	0.1577	3.3	0.0231	1.3	0.40	147.2	1.9	148.7	4.5	172.4	69.8	147.2	1.9
20	375	6100	2.4	0.1646	3.1	0.0243	1.0	0.32	154.5	1.5	154.7	4.5	158.0	69.0	154.5	1.5
21	373	4585	2.0	0.1585	4.9	0.0236	1.0	0.20	150.3	1.5	149.4	6.8	136.3	113.5	150.3	1.5
22	332	3820	1.7	0.1691	2.9	0.0239	1.3	0.46	152.5	2.0	158.6	4.3	252.0	59.3	152.5	2.0
23	622	7609	2.3	0.1592	2.8	0.0231	2.2	0.78	147.2	3.2	150.0	3.9	195.1	40.7	147.2	3.2
24	339	3368	3.0	0.1665	3.5	0.0239	1.0	0.28	152.4	1.5	156.4	5.1	216.4	78.3	152.4	1.5
25	316	7031	3.9	0.1626	2.9	0.0241	1.0	0.34	153.3	1.5	152.9	4.1	147.8	64.0	153.3	1.5
26	268	6523	3.7	0.1632	4.2	0.0241	2.7	0.65	153.2	4.1	153.5	6.0	157.8	75.6	153.2	4.1
27	406	7959	2.4	0.1641	2.7	0.0239	1.6	0.61	152.3	2.4	154.3	3.8	185.1	49.6	152.3	2.4
28	362	66479	5.2	0.8130	2.3	0.0988	1.0	0.44	607.3	5.8	604.1	10.3	592.3	43.9	607.3	5.8
29	326	5010	3.2	0.1629	8.8	0.0238	2.1	0.24	151.9	3.1	153.2	12.5	174.1	200.2	151.9	3.1
30	307	6586	3.6	0.1644	3.5	0.0243	1.2	0.35	155.0	1.9	154.5	5.1	147.5	77.6	155.0	1.9
31	292	4602	3.2	0.1632	4.0	0.0239	1.1	0.27	152.0	1.7	153.5	5.7	177.5	90.5	152.0	1.7
32	292	4602	3.2	0.1632	4.0	0.0239	1.1	0.27	152.0	1.7	153.5	5.7	177.5	90.5	152.0	1.7

as the fusion contact microstructure observed in feldspars. Other evidences are the common high-temperature and solid-state microstructures (Vernon, 2000) observed as chessboard extinction in quartz (Mainprice *et al.*, 1986), flame perthites in potassic feldspar (Vernon, 1999), and boudinage in hornblende (Hacker and Christie, 1990).

These mesoscale and microscale observations imply that the Kt dikes and the Kg1 and Kg2 units experienced a transition from magmatic, melt-supported flow to solid-state, grain-supported flow prior to their complete crystallization (submagmatic flow; Paterson *et al.*, 1998; Vernon, 2004). Such submagmatic flow, in addition to their persistent NW-SE orientation and NE-SW-directed lineation (Figures 3g and 3i), further suggests that those felsic units were more or less coeval, and linked together under a single deformational event.

Field observations indicate that the generation of the felsic units started with the emplacement of the Kt unit. In

contrast to the Kt dikes which display intense internal fabrics, the Kt massive body exhibits clear magmatic fabrics in the mesoscale (Figures 4b and 4c) and different structural patterns (compare Figure 3e with Figures 3f and 3h). Thus, because deformation is particularly well recorded in the Kt dikes, and in the Kg1 and Kg2 bodies as well, we propose that the emplacement of the 108.4 ± 2.2 Ma old Kt massive body marks the beginning of increasing strain rates, and therefore the initiation of the NE-side up deformational event.

The time interval and shear sense of the deformational event reported here is comparable to the intense ductile deformation that, according to Johnson *et al.* (1999) and Alsleben *et al.* (2008), mainly occurred between *ca.* 115 and 108 Ma in Sierra San Pedro Mártir (Figure 1a; locality SSPM), and between *ca.* 115 and 95 Ma in Calamajué (Figure 1a; locality 5), respectively.

The emplacement of the Kg3 dikes was the last intrusive event. These dikes have distinct orientations relative to the Kt dikes and the Kg1 and Kg2 bodies (compare Figure 3j with Figures 3f and 3h), distinct REE patterns (Figure 8b), and less intense solid-state microstructures relative to the Kg1 unit. These observations suggest that the emplacement of the Kg3 unit may coincide with the decrease of the strain rates and/or the presence of a different stress regime.

SUMMARY AND CONCLUSIONS

The 139.5 ± 2.0 Ma U-Pb zircon age of the hosting volcanic breccia from the northern part of the suite is contemporaneous with the lower member of the Eugenia Formation located in the Vizcaíno peninsula and the flysh-like assemblages of the PRB transitional zone. In turn, the 151.6 ± 2.6 Ma old granitoid (Jt unit) located in the southern part of the suite is coeval with the San Andrés-Cedros volcano-plutonic. However, north of Punta Prieta (Figure 1b), plutonic rocks of the PRB intrude the Cretaceous Alisitos Formation, which indicates that the Nuevo Rosarito plutonic suite is located near a boundary between the Cretaceous arc, represented by the Alisitos Formation, and a Jurassic arc, represented by a volcano-plutonic sequence that is contemporaneous to the San Andrés complex in the Vizcaíno peninsula.

Field relationships and structural analyses suggest that the deformational event responsible for the overturning of the host rocks and their intense internal fabrics occurred prior to the Cretaceous emplacement of the Nuevo Rosarito plutonic suite.

Nuevo Rosarito has geochemical characteristics similar to the western zone of the Peninsular Ranges batholith. Their intrusive units have a wide compositional range and a emplacement history that is separated into two phases. The first phase is defined by the emplacement of the mafic units, particularly, to the late crystallization of the gabbro and its fracturation under an extensional stress regime.

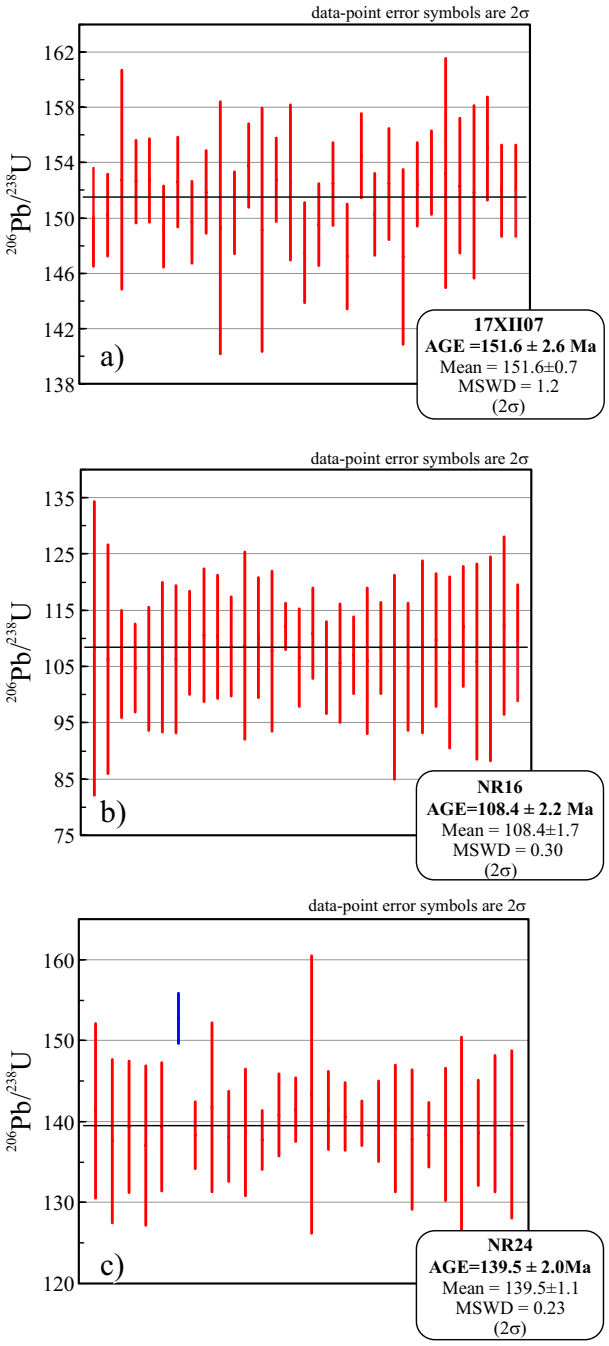

Figure 11. Single zircon $^{206}Pb/^{238}U$ ages of: (a) sample 17XII07 from a granitoid (Jt) hosting the southern part of the suite; (b) sample NR16 of the Kt massive body; and (c) sample NR24 of volcanic breccia hosting the northern part of the suite.

We propose that this promoted a local pressure contrast that drew the gabbroic residual melt to produce the NNE-oriented diorite bodies. The second phase is defined by the emplacement of the felsic units, particularly when a NE-side up deformational event occurred just after the emplacement of the 108.4 Ma old Kt massive body. This event was mainly recorded by the Kt dikes and the Kg1 and Kg2 bodies. The emplacement of the Kg3 dikes would indicate the end of the deformational event.

ACKNOWLEDGEMENTS

This paper was benefited from several discussions with colleagues at CICESE, including J. Fletcher, F. Suárez, A. Martín-Barajas, and O. Terán. We thank P. Montecinos, J. Estrada, G. Villalobos, and J. Contreras for comments on an early draft of the paper, Gabriel Rendón, Víctor Pérez, Susana Rosas, and Luis Gradilla for their technical support, and Emmanuelle Frery, Doris Piñeiro, Román Manjarrez, Porfirio Avilez and Patricia Juárez for joining us during fieldwork. Also thanks to Joaquin Ruiz and George Gehrels for allowing us the use of the LA-ICP-MS facilities at the Department of Geosciences, University of Arizona at Tucson, and to Felipe Escalona for his help during the LA-ICPMS measurements. Financial support was mostly provided by the project CONACyT 45817 granted to Luis Delgado, and by PAICYT-UANL CT131-09 granted to Fernando Velasco.

REFERENCES

Alsleben, H., Wetmore, P.H., Schmidt, K.L., Paterson, S.R., Melis, E.A., 2008, Complex deformation during arc continent collision: Quantifying finite strain in the accreted Alisitos arc, Peninsular Ranges batholith, Baja California: Journal of Structural Geology, 30, 220-236.

Anderson, E.M., 1938, The dynamics of sheet intrusion: Proceedings of the Royal Society of Edinburgh, 58, 242-251.

Anderson, E.M., 1951, The dynamics of faulting: Edinburgh, Oliver and Boyd, 206 pp.

Barnes, D.A., 1984, Volcanic arc derived, Mesozoic sedimentary rocks, Vizcaino Peninsula, Baja California Sur, Mexico, *in* V.A. Frizzell (ed.), Geology of the Baja California Peninsula: Society of Economic Paleontologists and Mineralogists, Pacific Section, 39, 119-130.

Barros, C.E.M., Barbey, P., Boullier, A.M., 2001, Role of magma pressure, tectonic stress and crystallization progress in the emplacement of the syntectonic A-type Estrela Granite Complex (Carajás Mineral Province, Brazil): Tectonophysics, 343, 93-109.

Bea, F., 1996, Residence of REE, Y, Th and U in Granites and Crustal Protoliths; Implications for the Chemistry of Crustal Melts: Journal of Petrology, 37, 521-552.

Beggs, J.M., 1984, Volcaniclastic rocks of the Alisitos Group, Baja California, Mexico, *in* Frizzell Jr., V.A. (ed.), Geology of the Baja California Peninsula: Society of Economic Paleontologists and Mineralogists, Pacific Section, Field Trip Guidebook, book 39, 1-7.

Bouchez, J.L., Delas, C., Gleizes, G., Nédélec, A., Cuney, M., 1992, Submagmatic microfractures in granites: Geology, 20, 35-38.

Boullier, A.M., Bouchez, J.L., 1978, Le quartz en rubans dans les mylonites: Bulletin de la Société Geologique de France, 7(XX), 253-262.

Brown, M., Solar, G.S., 1998, Granite ascent and emplacement during contractional deformation in convergent orogens: Journal of Structural Geology, 20(9/10), 1365-1393.

Busby, C.J., Fackler A.B., Mattinson, J., De Oreo, S., 2006, View of an intact oceanic arc, from surficial to mesozonal levels: Cretaceous Alisitos Arc, Baja California, Mexico: Journal of Volcanology and Geothermal Research, 149, 1-46.

Camarena-García, M.A., 2006, Análisis morfológico y estructural de los complejos plutónicos de Baja California Central a través de las técnicas de percepción remota: Ensenada, México, Centro de Investigación Científica y de Estudios Superiores de Ensenada (CICESE), tesis de maestría, 112 pp.

Coleman, D.S., Gray, W., Glazner, A.F., 2004, Rethinking the emplacement and evolution of zoned plutons: Geochronologic evidence for incremental assembly of the Tuolumne Intrusive Suite, California: Geology, 32, 433-436.

Comisión de Estudios del Territorio Nacional (CETENAL), 1977, Mapa geológico Rosarito H11D69, escala 1:50000: México, D.F., Instituto Nacional de Estadística, Geografía e Informática (INEGI), 1 mapa.

Cox, K.G., Bell, J.D., Pankhurst, R.J., 1979, The Interpretation of Igneous Rocks, George Allen and Unwin, 450 pp.

Delgado-Argote, L.A., 2000, Evolución Tectónica y Magmatismo Neógeno de la Margen Oriental de Baja California Central: México, D.F., Universidad Nacional Autónoma de México (UNAM), tesis doctoral, 194 pp.

DePaolo, D.J., 1981, A Neodymium and Strontium Isotopic Study of the Mesozoic Calc-Alkaline Granitic Batholiths of the Sierra Nevada and Peninsular Ranges, California: Journal of Geophysical Research, 86, 10470-10488.

D'Lemos, R.S., Brown, M., Strachan, R.A., 1992, Granite magma generation, ascent and emplacement within a transpressional orogen: Journal of Geological Society, 149, 487-490.

Fournelle, J., Marsh, B.D., 1991, Shishaldin Volcano: Aleutian high-alumina basalts and the question of plagioclase accumulation: Geology, 19, 234-237.

Frost, B.R., Barnes, C.G., Collins, W.J., Arculus, R.J., Ellis, D.J., Frost, C.D., 2001, A geochemical classification for granitic rocks: Journal of Petrology, 42, 2033–2048.

Gastil, R.G., 1993, Prebatholithic history of peninsular California, *in* Gastil, R.G., and Miller, R.H. (eds.), The prebatholithic stratigraphy of peninsular California: Boulder, Colorado, Geological Society of America Special Paper 279, 145–156.

Gastil, R.G., Miller, R.H., 1984, Prebatholithic paleogeography of peninsular California and adjacent Mexico, *in* Frizzel, V.A. (ed.), Geology of the Baja California peninsula: Society of Economic Paleontologists and Mineralogists, Pacific Section, 9-16.

Gastil, R.G., Phillips, R.P., Allison, E.C., 1975, Reconnaissance geology of the State of Baja California: Geological Society of America Memoir 140, 170.

Gastil, R.G., Diamond, C.K., Walawender, M.J., Marshal, M., Boyles, C., Chadwick, B., 1990, The problem of the magnetite/ilmenite boundary in southern and Baja California, *in* Anderson, J.L. (ed.), The Nature and Origin of Cordilleran Magmatism: Boulder, Colorado, Geological Society of America Memoir 174, 19-32.

Gastil, R.G., Kimbrough, J., Shimizu, M., Tainosho, Y., 1994, Origin of the magnetite boundary in the Peninsular Ranges batholith, Southern California, U.S.A., and Baja California, México: Revista Mexicana de Ciencias Geológicas, 11(2), 157-167.

Gehrels, G., Valencia, V., Pullen, A., 2006, Detrital Zircon Geochronology by Laser Ablation Multicollector ICPMS at the Arizona LaserChron Center, *in* Olszewski, T. (ed.), Geochronology: Emerging Opportunities: Paleontology Society Papers, 12, 67-76.

Gehrels, G., Valencia, V., Ruiz, J., 2008, Enhanced precision, accuracy, efficiency, and spatial resolution of U-Pb ages by laser ablation–multicollector–inductively coupled plasma–mass spectrometry: Geochemistry Geophysics Geosystems, 9, Q03017.

Geshi, N., 2001, Melt segregation by localized shear deformation and fracturing during crystallization of magma in shallow intrusions of the Otoge volcanic complex, central Japan: Journal of Volcanology and Geothermal Research, 106, 285-300.

Gromet, L.P., Silver, L.T., 1987, REE variations across the Peninsular Ranges batholith: Implications for batholithic petrogenesis and crustal growth in magmatic arcs: Journal of Petrology, 28, 77-125.

Hacker, B.R., Christie, J.M., 1990, Brittle/ductile and plastic/cataclastic transitions in experimentally deformed and metamorphosed amphibolites: American Geophysical Union Monograph 56, 127-147.

Haskin, L., Haskin, M., Frey, F., Wildeman, T., 1968, Relative and absolute terrestrial abundances of the rare earths, *in* Ahrens L.

(ed.), Origin and Distribution of the Elements: Oxford, Pergamon Press, 889-912.

Hibbard, M.J., Waters, R.J., 1985, Fracturing and diking in incompletely crystallized granitic plutons: Lithos, 18, 1-12.

Hickey, J., 1984, Stratigraphy and composition of a Jura-Cretaceous volcanic arc apron, Punta Eugenia, Baja California Sur, Mexico, *in* Frizzell, V.A.,Jr., (ed.), Geology of the Baja California peninsula: Field Trip Guidebook-Pacific Section: Society of Economic Paleontologists and Mineralogists, Pacific Section, 39, 149-160.

Hongo, Y., Obata, H., Gamo, T., Nakaseama, M., Ishibashi, J., Konno, U., Saegusa, S., Ohkubo, S., Tsunogai, U., 2007. Rare Earth Elements in the hydrothermal system at Okinawa Trough back-arc basin: Geochemical Journal, 41, 1-15.

Johnson, S.E., Tate, M.C., Fanning, C.M., 1999, New geological and SHRIMP U-Pb zircon data in the Peninsular Ranges batholith, Baja California, México: Evidence for a suture?: Geology, 27, 743-746.

Johnson, S.E., Schmidt, K.L., Tate, M.C., 2002, Ring complexes in the Peninsular Ranges Batholith, Baja California, México and southern California, USA: middle- to upper-crustal magma plumbing systems: Lithos, 61, 187-208.

Kemp, A.I.S., Hawkesworth, C.J., Foster, G.L., Paterson, B.A., Woodhead, J.D., Hergt, J.M., Gray, C.M., Whitehouse, M.J. 2007, Magmatic and crustal differentiation history of granitic rocks from Hf-O isotopes in zircon: Science, 315, 980-983.

Kimbrough, D.L., Moore, T.E., 2003, Ophiolite and volcanic arc assemblages on the Vizcaino Peninsula and Cedros Island, Baja California Sur, Mexico: Mesozoic forearc lithosphere of the Cordilleran magmatic arc, *in* Johnson, S.E., Paterson, S.R., Fletcher, J., Girty, G.H., Kimbrough, D.L., Martín-Barajas, A. (eds.), Tectonic evolution of northwestern Mexico and the southwestern USA: Geological Society of America Special Paper 374. 43-72.

Ludwig, K.J., 2003. Isoplot ver. 3.00: Berkeley, Berkeley Geochronology Center, Special Publication 4, 70 pp.

Mainprice, D., Bouchez, J.L., Blumenfeld, P., Tubia, J.M., 1986, Dominant c slip in naturally deformed quartz: implications for dramatic plastic softening at high temperature: Geology, 14, 819-822.

Martín-Barajas, A., Delgado-Argote, L.A., 1996, Monografía Geológico Minera de Baja California: Baja California, México, Secretaría de Desarrollo Económico, 107 pp.

Matzel, J.E.P., Bowring, S.A., Miller, R.B., 2006, Time scales of pluton construction at differing crustal levels: Examples from the Mount Stuart and Tenpeak intrusions, North Cascades, Washington: Geological Society of America Bulletin, 118, 1412-1430.

Michel, J., Baumgartner, L., Putlitz, B., Schaltegger, U., Ovtcharova, M., 2008, Incremental growth of the Patagonian Torres del Paine laccolith over 90 k.y.: Geology, 36, 459-462.

Middlemost, E.A.K., 1989, Iron oxidation ratios, norms and the classification of volcanic rocks: Chemical Geology, 77, 19-26.

Nakamura, N., 1974, Determination of REE, Ba, Fe, Mg, Na and K in carbonaceous and ordinary chondrites: Geochimica et Cosmochimica Acta, 38, 757-775.

Park, Y., Means D., 1996, Direct observation of deformation processes in crystal mushes: Journal of Structural Geology, 18, 847-858.

Paterson, S.R., Fowler Jr., T.K., Schmidt, K.L., Yoshinobu, A.S., Yuan, E.S., Miller, R.B., 1998, Interpreting magmatic fabric patterns in plutons: Lithos, 44, 53-82.

Rubatto, D., 2002, Zircon trace element geochemistry: partitioning with garnet and the link between U-Pb ages and metamorphism: Chemical Geology, 184, 123-138.

Sawyer, E.W., 2001, Melt segregation in the continental crust: Distribution and movement of melt in anatectic rocks: Journal of Metamorphic Geology, 19, 291-309.

Schmidt, K.L., Wetmore, P.H., Johnson, S.E., Paterson, S.R., 2002, Controls on orogenesis along an ocean-continent margin transition in the Jura-Cretaceous Peninsular Ranges batholith, *in* Barth, A. (ed.), Contributions to Crustal Evolution of the Southwestern United States: Boulder, Colorado, Geological Society of America Special Paper 365, 49-71.

Shervais, J.W., 1982, Ti-V plots and the petrogenesis of modern and ophiolitic lavas: Earth and Planetary Science Letters, 59, 101-118.

Silver, L.T., Chappell, B., 1988, The Peninsular Ranges batholith: An insight into the Cordilleran batholiths of southwestern North America: Transactions of the Royal Society of Edinburgh, Earth Sciences, 79, 105-121.

Stacey, J.S.K., Kramers, J.D., 1975, Approximation of terrestrial lead isotope evolution by a two-stage model: Earth and Planetary Science Letters, 26, 207-221.

Streckeisen, A.L., 1976, To each plutonic rock its proper name: Earth Science Reviews, 12, 1-33.

Tate, M.C., Norman, D.C., Johnson, S.E., Fanning, C.M., Anderson, J.L., 1999, Generation of Tonalite and Trondhjemite by Subvolcanic Fractionation and Partial Melting in the Zarza Intrusive Complex, Western Peninsular Ranges Batholith, Northwestern Mexico: Journal of Petrology, 40, 983-1010.

Terra Softa, Inc., 2009, IGPET for Windows, Manual, 49 pp.

Todd, V.R., Shaw, S.E., 1985, S-type granitoids and an I-S line in the Peninsular Ranges batholith, southern California, Geology, 13, 231-233.

Tulloch, A.J., Kimbrough, D.L., 2003, Paired plutonic belts in convergent margins and the development of high Sr/Y magmatism: Peninsular Ranges batholith of Baja-California and Median batholith of New Zealand, *in* Johnson, S.E., Paterson, S.R., Fletcher, J., Girty, G.H., Kimbrough, D.L., Martín-Barajas, A. (eds.), Tectonic Evolution of Northwestern Mexico and the Southwestern USA: Geological Society of America Special Paper 374, 275–295.

Valencia, V.A., Barra F., Weber B., Ruiz J., Geherls G., Chesley J., Lopez Martinez M. 2006, Re-Os and U-Pb geochronology of the El Arco Porphyry copper deposit, Baja California Mexico: Journal of South American Earth Sciences, 22, 39-51.

Verma, S.P., Torres-Alvarado, I.S., Velasco-Tapia, F., 2003, A revised CIPW norm: Schweizerische Mineralogische und Petrographische (Swiss Bulletin of Mineralogy and Petrology), 83, 197-216.

Vernon, R.H. 1999, Flame perthite in metapelitic gneisses in the Cooma Complex, SE Australia: American Mineralogist, 84, 1760-1765.

Vernon, R.H., 2000, Review of microstructural evidence of magmatic and solid-state flow: Electronic Geosciences, 5, 2.

Vernon, R.H., 2004, A Practical Guide to Rock Microstructure: Cambridge University Press, 594 pp.

Vigneresse, J.L., 2004, A new paradigm for granite generation: Transactions of the Royal Society of Edinburgh, 95, 11-22.

Walawender, M.J., Smith, T.E., 1980, Geochemical and petrologic evolution of the basic plutons of the Peninsular Ranges batholith, southern California: Journal of Geology, 88, 233-242.

Walawender, M.J., Gastil, R.G., Clinkenbeard, W.V., McCormick, W.V., Eastman, B.G.,Wernicke, M.S.,Wardlaw, M.S., Gunn, S.H., Smith, B.M., 1990, Origin and evolution of the zoned La Posta–type plutons, eastern Peninsular Ranges batholith, southern and Baja California, *in* Anderson, J.L. (ed.), The Nature and Origin of Cordilleran Magmatism: Boulder, Colorado, Geological Society of America Memoir 174, 1–18.

Weber B., Lopez Martinez M., 2006, Pb, Sr, and Nd isotopic and chemical evidence for a primitive island arc emplacement of the El Arco porphyry copper deposit (Baja California, Mexico): Mineralium Deposita, 40, 707-725.

Wilson, M., 1989, Igneous Petrogenesis: A global tectonic approach: London, Chapman & Hall, 466 pp.

Manuscript received: May 16, 2011
Corrected manuscript received: August 23, 2011
Manuscript accepted: September 5, 2011